Petrological insights into magma storage and evolution at Rabaul Caldera, Papua New Guinea

Melina Höhn[1*], Margaret Hartley[1], John B. Dikaung[2], Ima Itikarai[2], Kila Mulina[2], Steve Saunders[2], Mikhail Sindang[2], Brendan McCormick Kilbride[1]

[1]*Department of Earth and Environmental Sciences, University of Manchester, Manchester, M13 9PL, United Kingdom*

[2]*Rabaul Volcano Observatory, P.O. Box 386, Rabaul, East New Britain Province, Papua New Guinea*

*Corresponding author. E-mail: melina1995.hoehn@gmail.com

This is a non-peer reviewed preprint submitted to EarthArXiv in January 2026. It has also been submitted for publication to *Journal of Petrology* and is currently under review. Subsequent versions may differ.

Petrological insights into magma storage and evolution at Rabaul Caldera, Papua New Guinea

Melina Höhn[1*], Margaret Hartley[1], John B. Dikaung[2], Ima Itikarai[2], Kila Mulina[2], Steve Saunders[2], Mikhail Sindang[2], Brendan McCormick Kilbride[1]

[1]*Department of Earth and Environmental Sciences, University of Manchester, Manchester, M13 9PL, United Kingdom*

[2]*Rabaul Volcano Observatory, P.O. Box 386, Rabaul, East New Britain Province, Papua New Guinea*

*Corresponding author. E-mail: melina1995.hoehn@gmail.com

Abstract

Rabaul is a caldera volcano in Papua New Guinea. Its most recent caldera-forming eruption occurred ~1400 years ago, with numerous intra-caldera eruptions since. Erupted whole rock compositions are commonly attributed to fractional crystallisation along a single liquid line of descent, but mafic mineral clots indicate mafic recharge and magma mixing also influence whole rock compositions. Geophysical studies identified two low-velocity zones at ~0.5–4 km and 9–15 km beneath the caldera, suggesting a shallow reservoir for evolved magmas and a deeper mafic storage zone. However, uncertainties remain regarding depths, connectivity and temporal evolution of Rabaul's magma storage zones. We present petrological and thermobarometric analyses of products from the 1937, 1994 and 2014 eruptions at Rabaul. Samples contain two distinct mineral clot types. Mafic mineral clots comprise olivine, high-

anorthite plagioclase and high-Mg# clinopyroxene that are out of equilibrium with surrounding matrix glass. Textures include rapid growth rims, olivine replacement by orthopyroxene and reversely zoned clinopyroxene. We interpret these mafic mineral clots as cumulate fragments mobilised from a deep mafic mush by mafic recharge. Intermediate mineral clots contain low-anorthite plagioclase, low-Mg# clinopyroxene, orthopyroxene and Ti-magnetite, and occur as macrocrysts in equilibrium with matrix glasses (Mg# 30–40). We interpret these intermediate mineral clots as fragments from a shallower, more evolved mush stored. Binary mixing models demonstrate that eruption products can be reproduced by mixing a mafic magma similar to 1937 basaltic enclaves with a dacitic magma resembling the last caldera-forming deposit. Clinopyroxene-only and clinopyroxene–liquid thermobarometry yield crystallisation pressures of 0.5–5 kbar (~2–20 km) and temperatures of 960–1125 °C, but the models lack the vertical resolution to resolve storage zones separated by ~5 km. Combining geophysical, geochemical and thermobarometric data we propose a refined model of magma storage beneath Rabaul, in which magmas are stored in a complex, vertically extensive magma plumbing system with a heterogeneous but interconnected mush reservoir.

Key Words: magma mixing; magma recharge; magma storage; Rabaul; thermobarometry

Introduction

Magma reservoirs in arc settings exhibit diverse geometries, influenced by factors such as crustal thickness, magma supply rate, and thermal conditions (Edmonds *et al.*, 2019, Sparks *et al.*, 2019). The current view on magma reservoirs in the crust is that they exist as interconnected networks of melt-rich zones within a crystal mush framework (Annen *et al.*, 2006, Edmonds *et al.*, 2019, Horn *et al.*, 2022). Seismic tomography reveals that many reservoirs are vertically extensive throughout the crust, with multiple storage levels (Delph *et al.*, 2017, Paulatto *et al.*, 2019). Many arc volcanoes exhibit complex magmatic processes such as magma mixing and mafic recharge which occur when a hotter, more primitive magma intrudes into a shallower, cooler, more evolved magma reservoir (Anderson, 1976, Cashman & Sparks, 2013). Mafic recharge events are often implicated in triggering volcanic eruptions by injecting heat and volatiles into a resident magma body, thereby reducing its density and increasing its buoyancy (Mangler *et al.*, 2022, Sparks & Marshall, 1986, Sparks *et al.*, 1977). Understanding how these recharge events fit within the broader framework of an arc volcano's magma plumbing system is essential, as these interconnected reservoirs at various depths regulate magma storage, transport, and eruption dynamics (Mangler *et al.*, 2022, Takach *et al.*, 2024, Viccaro *et al.*, 2012).

Rabaul is an arc volcano located on the eastern tip of the island of New Britain, Papua New Guinea. Rabaul is characterised by a complex 330 kyr-long eruption history with several caldera-forming eruptions as well as smaller eruptions from multiple post-caldera vents (Nairn *et al.*, 1995, Patia, 2004, Wood *et al.*, 1995). The majority of volcanic rocks from Rabaul plot along a linear trend on TAS and other major element diagrams, a trend commonly referred to in the literature as the "main series" (Patia, 2004, Wood *et al.*, 1995). This linear trend has

previously been interpreted as representing a single liquid line of descent controlled by fractional crystallisation (Heming, 1974, Patia, 2004, Wood *et al.*, 1995). However, additional processes such as variable degrees of melting of geochemically distinct mantle sources (Grove *et al.*, 2002), crustal assimilation (Hildreth & Moorbath, 1988, Mason *et al.*, 1996), and magma mixing (Reubi & Blundy, 2009, Ruprecht *et al.*, 2012) can generate geochemical diversity, producing compositional series that do not necessarily reflect simple fractional crystallisation trends (Namur *et al.*, 2020). Indeed, mafic mineral clots (aggregates of two or more crystals) in the Rabaul eruption products have been interpreted as mafic enclaves introduced by recharge processes. These mafic mineral clots have been taken as evidence that magma mixing is an important process influencing the range of whole rock compositions shown by Rabaul's eruption products (Bouvet de Maisonneuve *et al.*, 2015, Fabbro *et al.*, 2020, Patia *et al.*, 2017). This is supported by previous mixing modelling by Patia et al. (2017) and Fabbro et al. (2020) who show that the whole rock compositions from the 1994 and 2014 eruptions could have been formed by mixing basaltic and dacitic magma. However, critical questions remain about the specific endmember compositions driving mixing processes at Rabaul.

Geophysical imaging reveals the presence of two distinct low velocity zones at depths of around 0.5–4 km and around 9–15 km beneath the Rabaul Caldera (Bai & Greenhalgh, 2005, Finlayson *et al.*, 2003, Itikarai, 2008). This may indicate the existence of a shallow magma reservoir where magmas accumulate prior to intra-caldera eruptions and a deeper region of the magma plumbing system that may store more mafic recharge magmas. A range of mineral-melt and mineral-only thermobarometer have been used to calculate magma storage and crystallisation conditions of ~930°C and ≤2 kbar for the 2006 eruption products (Bouvet de Maisonneuve *et al.*, 2015) and 970–1020°C and 0.4–4 kbar for the 2014 eruptives (Fabbro et al., 2020). These calculation outputs recover shallow magma storage conditions similar to the

geophysical estimates, but do not recover signatures of crystallisation in a deeper reservoir. The considerable range in pressure and temperature conditions recovered by thermobarometry calculations demonstrate that considerable uncertainty remains regarding the depth, connectivity, and temporal evolution of Rabaul's magma storage zones.

Despite past geochemical studies using whole rock data, there have been no detailed studies of the chemical and petrological characteristics of the phenocryst cargoes of Rabaul erupted products thought to be generated by magma mixing. A comprehensive chemical and petrographic investigation of eruptive products from multiple Rabaul eruptions would substantially improve our understanding of the magmatic processes operating within the Rabaul magma plumbing system. In particular, detailed characterisation of zoning patterns in phenocrysts can constrain temporal variations in temperature, pressure and melt composition, and thus illuminate the temporal evolution and dynamic behaviour of the reservoir (Morgavi *et al.*, 2022, Palummo *et al.*, 2021, Streck, 2008, Ubide *et al.*, 2021).

In this study, we provide a detailed study of mineral zoning patterns and compositional characteristics of samples from the 1937, 1994, and 2014 eruptions at Rabaul to provide insights into the temporal evolution of Rabaul's magma supply and to distinguish between the chemical signatures of fractional crystallisation, mafic recharge, and magma mixing. Additionally, we use the newer clinopyroxene-only and clinopyroxene–liquid thermobarometry models of Jorgenson *et al.* (2022) and Petrelli *et al.* (2020) to try to improve our picture on the vertical extent of the Rabaul magma plumbing system. Lastly, we provide the first quantification of the oxygen fugacity of Rabaul magmas through oxybarometry, offering novel insights into the system's redox state. By combining mineral chemistry, textural analysis, and thermobarometric constraints, our research sheds new light on transcrustal

magma storage and remobilisation dynamics underneath the Rabaul Caldera and contributes to a refined model of the Rabaul magma plumbing system.

Geological background

Tectonic and geographic background

Rabaul is located on the Gazelle Peninsula, northeastern New Britain, positioned within the complex tectonic environment of the converging Pacific and Australian plates (Baldwin *et al.*, 2012, Holm *et al.*, 2016) (Fig. 1a). New Britain forms part of the New Britain volcanic arc, which formed in response to the subduction of the Solomon Sea plate beneath the Bismarck Sea plate at the New Britain Trench (Baldwin *et al.*, 2012, Holm *et al.*, 2016).

The Rabaul caldera measures 14×9 km and is largely flooded by Blanche Bay (Heming, 1974, Nairn *et al.*, 1995) (Fig. 1b). The caldera formed around 1400 years ago during a major eruption, referred to as the Rabaul Pyroclastics eruption (McKee *et al.*, 2015). The Gazelle Peninsula is densely populated, with the town of Rabaul historically serving as the provincial capital before being heavily damaged by volcanic eruptions, the last time in 1994 (Johnson, 2013b). The modern capital Kokopo remains at risk from higher intensity eruptions of Rabaul.

To the east of the caldera lie the relatively little-eroded stratovolcanoes Kombiu and Turangunan, and the heavily eroded and breached volcano Palangiangia within which the younger cone of Rabalanakaia has grown (Fig. 1b). These edifices, together with the northern volcanoes of Tovanumbatir and Watom Island, belong to the so-called Watom-Turangunan-Zone (WTZ), a NW-SE trending zone of predominantly mafic stratovolcanoes (Heming, 1974, McKee & Duncan, 2016). The most active vents within Rabaul caldera in recent history have

been Vulcan and Tavurvur, located on the western and eastern sides of the caldera floor, respectively. These vents have been the source of the most recent explosive eruptions in 1937, 1994, 2006 and 2014 (Heming, 1974, Nairn *et al.*, 1995, Nairn *et al.*, 1989, Patia, 2004).

Eruption history of Rabaul

Volcanism at Rabaul started >330 kyr ago and includes at least ten dacitic ignimbrite-producing eruptions, some of which were caldera-forming (McKee & Duncan, 2016, Nairn *et al.*, 1995, Nairn *et al.*, 1989, Wood *et al.*, 1995). The Rabaul Pyroclastics eruption, which occurred between 667 and 699 CE (McKee *et al.*, 2015), is thought to have produced extensive pyroclastic flows and tephra deposits that covered much of the northeastern Gazelle Peninsula. Since this major event, Rabaul has undergone several smaller intra-caldera eruptions of VEI ≤4 (Nairn *et al.*, 1995, Nairn *et al.*, 1989, Wood *et al.*, 1995) (Table 1). This study focuses on eruptive activity since 1937.

In 1937, a twin eruption occurred at both Vulcan and Tavurvur (Patia, 2004). This explosive eruption was the result of interaction with seawater and was assigned a VEI of 4 (Patia, 2004, Roggensack *et al.*, 1996). The twin eruption ejected large volumes of ash and pumice leading to the build-up of a 255 m-high cone that linked the previous Vulcan Island to the mainland. The main phase of activity at both vents ended on 2 June 1937 but some isolated vulcanian explosions continued at Tavurvur until 1943 (Patia, 2004).

After four decades of quiescence, Rabaul experienced a period of significant seismic activity and ground deformation in 1983–1985 (McKee *et al.*, 1984, Mori & McKee, 1987). The seismic epicentres formed a ring pattern tracing the outline of the Rabaul Pyroclastics caldera

(Mori & McKee, 1987). These phenomena were interpreted as intrusion of magma beneath the caldera, leading to concerns that an eruption was imminent (Mori & McKee, 1987, Saunders, 2001). However, no eruption occurred.

A further twin eruption of Vulcan and Tavurvur occurred in 1994. This eruption was preceded by near-continuous seismic activity of fluctuating intensity (maximum of M_L 5.1) starting on 18 September (Global Volcanism Program, 1994a). Tilt meters recorded uplift of up to 6 m at Vulcan, which resulted in a shift in the southern shoreline to the south by ~70 m (Global Volcanism Program, 1994a). The eruption started on 19 September. Volcanic activity at Vulcan was short-lived and involved a Plinian-style eruption, whereas the volcanic activity at Tavurvur comprised less powerful, but more sustained strombolian activity (Global Volcanism Program, 1994a, Global Volcanism Program, 1994b). The 1994 eruption devastated the town of Rabaul, burying much of the infrastructure under meters of ash and forcing the evacuation of tens of thousands of residents (Global Volcanism Program, 1994a, Johnson, 2013a). The twin eruption produced pyroclastic flows, widespread ashfall, and volcanic lightning, disrupting life on the Gazelle Peninsula. Despite the extensive damage, the 1994 eruption resulted in few fatalities, largely due to successful evacuation efforts (Fearnley *et al.*, 2018, Global Volcanism Program, 1994a, Johnson, 2013a).

Following the 1994 event, Rabaul entered a phase of intermittent eruptive activity, with periodic explosions, lava dome growth in Tavurvur's crater, and small-to-moderate ash emissions. Discrete, stronger eruptions occurred in 2006 and 2014. The 2006 eruption of Tavurvur started on 7 October and was characterised by ash emissions up to 18 km high and strombolian eruptions with lava effusion, but it did not result in significant damage to the surrounding region. Strombolian activity subsided by the evening of 7 October

(Global Volcanism Program, 2006). Mild volcanic activity continued again after November 2006 with periods of weeks to months of quiescence (Global Volcanism Program, 2007, Global Volcanism Program, 2011, Global Volcanism Program, 2013).

The most recent eruption of Tavurvur began on 29 August 2014. Volcanic activity started with a strombolian eruption which included discrete explosions with ejections of volcanic bombs 500–1000 m from the crater, small lava fountains, and an 18 km-high plume with extensive ash fall (Global Volcanism Program, 2014). Volcanic activity lasted ~24 hours with smaller explosions following until 30 August. The release of diffuse, white vapour, was recorded until 2021 (Global Volcanism Program, 2017). Renewed deformation with uplift of up to 39 mm/month and increased seismicity has been detected at Rabaul since September 2021 (Global Volcanism Program, 2021, Saunders *et al.*, 2023). By November 2024, this ongoing uplift has resulted in a cumulative vertical displacement of ~7 cm (Global Volcanism Program, 2024).

The 20th century eruptions at Rabaul underscore the ongoing volcanic hazards posed by this volcano, and the necessity for continuous monitoring. The persistence of unrest at Tavurvur in particular suggests that Rabaul remains a significant threat to the local population, with the potential for future explosive eruptions.

Analytical methods

Samples

We analysed one pumice sample from the 1937 eruption, one volcanic bomb and four lava samples from the 1994 eruption, and two volcanic bombs from the 2014 eruption (Table 2).

All samples are grey to dark grey in colour. They contain abundant macrocrysts (defined as crystals isolated in the matrix with size 0.5–2 mm) as well as crystal aggregates of sufficient size (0.5–1 cm) to be visible to the naked eye, hereafter referred to as mineral clots. The macrocrysts and mineral clots are embedded in a microcrystalline groundmass comprising clinopyroxene and plagioclase with interstitial glass. The vesicularity of the samples decreases from the pumice (~80 vol%) to the volcanic bombs (~60 vol%) to the lavas (~4–20 vol%).

Thin section maps

We prepared one to two thin sections from each sample and examined all thin sections under a polarising microscope to determine their characteristic mineral assemblage and texture. We conducted petrographic and mineralogical examinations using an FEI Quanta 650 Environmental FEG scanning electron microscope (SEM) at the Department of Earth and Environmental Sciences, University of Manchester, UK. We produced whole-thin-section-maps of representative samples depicting their mineralogy and texture (Figs. A.1–A.4). We first acquired back-scattered electron (BSE) and energy-dispersive X-ray (EDX) maps using an SEM. We processed the EDX data using XMapTools software (Lanari *et al.*, 2023) to produce modal mineralogy maps, which were used to estimate mineral modal abundances and to support the investigation of mineralogy and textural variations within and between samples. Mineral classification was supported by targeted point analyses carried out by electron probe microanalysis (EPMA).

Whole rock analysis

For whole rock analysis, representative sample pieces from each deposit were crushed into <2 mm chips with a stainless steel mortar and then ground into powders using an agate ball

mill. Whole rock compositions were measured by X-ray Fluorescence (XRF) spectroscopy at ETH Zürich, Switzerland. We measured major element oxides SiO_2, TiO_2, Al_2O_3, Fe_2O_3, MnO, MgO, CaO, Na_2O, K_2O, P_2O5, Cr_2O_3, and NiO, and trace elements comprise Rb, Ba, Sr, Nb, Zr, Hf, Y, Ga, Zn, Cu, Ni, Co, Cr, V, Sc, La, Ce, Nd, Pb, Th, U, and W. Detailed information on the analytical procedure for XRF analysis can be found in the Supplementary File S1. All XRF data can be found in Supplementary File S2.

Electron probe microanalysis (EPMA)

We conducted electron microprobe analyses at the Department of Mineralogy, University of Münster, Germany and the Department of Earth and Environmental Sciences, University of Manchester, UK. We measured core and rim compositions of plagioclase, clinopyroxene, orthopyroxene, and olivine as well as matrix glass in all of the collected samples from Rabaul. Elements analysed were SiO_2, TiO_2, Al_2O_3, FeO^T, MnO, MgO, CaO, Na_2O, K_2O, P_2O5, Cr_2O_3, and NiO; CoO was included in olivine measurements. We used the optimised analytical set-up of Neave *et al.* (2024) for clinopyroxene analyses to minimise the analytical uncertainty on minor elements and improve precision of thermobarometry calculations (Neave *et al.*, 2024, Wieser *et al.*, 2023b). We also analysed Ti-magnetite in samples from each Rabaul eruption for oxybarometry. Here, the analysed elements were SiO_2, TiO_2, Al_2O_3, Fe_2O_3, FeO, MnO, MgO, CaO, Na_2O, K_2O, Cr_2O_3, NiO, ZnO, and V_2O_3. Detailed information on the analytical conditions for EPMA analysis can be found in the Supplementary File S1. All EPMA data can be found in Supplementary Files S3–S6.

Thermobarometry calculations

We performed clinopyroxene-only and clinopyroxene–liquid thermobarometry calculations using the open-source Python tool Thermobar (Wieser *et al.*, 2022). We applied the machine learning-based models developed by Jorgenson et al. (2022) and Petrelli et al. (2020), which produce the smallest mismatch between calculated and experimental pressures at the pressure-temperature-melt H_2O conditions relevant to arc settings (Wieser *et al.*, 2023a). All thermobarometry data can be found in Supplementary File S7.

For cpx-liquid thermobarometry, we first performed mineral-melt equilibrium matching. We tested clinopyroxene crystals for equilibrium against a dataset of putative liquid compositions comprising matrix glass and whole rock analyses based on the following equilibrium conditions. The equilibrium coefficient ($KD_{cpx\text{-}liq}^{Fe\text{-}Mg}$) between cpx and liquid was set at 0.27 with a 2σ error of 0.08. We considered glass and clinopyroxene to be in equilibrium when the observed DiHd, EnFs and CaTs component values were within ±0.12, ±0.10 and ±0.06 (2 SEE) for DiHd, EnFs and CaTs components, respectively (Neave *et al.*, 2019). For each equilibrium clinopyroxene-liquid pair, we calculated pressures and temperatures with the Jorgenson et al. (2022) and Petrelli et al. (2020) models. Pressure-temperature pairs with an interquartile range (IQR) of the voting distribution exceeding 6.8 were discarded, following the recommendation of Jorgenson et al. (2022). The same filtering criterion was applied to estimates derived from the Petrelli et al. (2020) model, due to the comparable standard error on the pressure. The mean and standard deviation of the pressure–temperature estimates were then determined for each clinopyroxene crystal. Pressures were subsequently converted to depths using the crustal density model of Rasmussen *et al.* (2022). In parallel, for cpx-only thermobarometry calculations, we calculated pressures and temperatures with the same models from Jorgenson et al. (2022) and Petrelli et al. (2020) for each individual clinopyroxene. Afterwards, we applied

the IQR >6.8 filter and converted pressures to depth using the crustal density model of Rasmussen *et al.* (2022).

We used a Monte Carlo error propagation implemented in Thermobar to estimate the analytical uncertainty associated with our clinopyroxene-liquid pressure-temperature estimates. We created a set of 20,000 theoretical mineral and melt compositions based on the 1σ analytical clinopyroxene and liquid errors from the EPMA measurements for one matching clinopyroxene and liquid pair for each Rabaul eruption. Afterwards, we calculated pressures and temperatures with the models from Jorgenson et al. (2022) and Petrelli et al. (2020) for each of the 20,000 matching clinopyroxene and liquid pairs. Supplementary Figure S1 shows the 67% and 95% contours which show the range of pressure-temperature estimates produced by 67% and 95% of the 20,000 theoretical clinopyroxene-liquid pairs. Analogous Monte Carlo calculations were run for the clinopyroxene-only models (Supplementary Fig. S2). The results show that propagated analytical uncertainty on a single clinopyroxene-liquid equilibrium pair can produce pressure-temperature estimates that vary by 25–100°C and ~0.5–3 kbar.

Oxygen fugacity calculations

We used the oxybarometer FETiMM (Arató & Audétat, 2017) to calculate the oxygen fugacity of magmas erupted in 1937, 1994 and 2014 at Rabaul. This oxybarometer uses the partitioning of Fe and Ti between magnetite and silicate melt to estimate fO_2. We analysed 20–32 Ti-magnetite crystals in one volcanic bomb or pumice sample from each eruption (samples 1937_pum_b, S152971a, S153126a, VB_IB02) and calculated the average compositions of the EPMA matrix analyses measured in each sample. The inputs for the oxybarometer are the Fe-Ti exchange coefficient between the magnetite and silicate melt, and the AMCNK component

(molar $Al_2O_3/(CaO+Na_2O+K_2O+MgO)$) of the melt compositions. Our calculations yield oxygen fugacity conditions of ΔQFM = +1.3 ±0.02 for the 1937 pumice, ΔQFM = +1.1 ±0.2 for the 1994 volcanic bombs, and ΔQFM = +0.9 ±0.1 for the 2014 volcanic bombs. The uncertainties calculated for individual eruptions are comparable with the oxybarometer uncertainty of ±0.2–0.3 log units fO2 at ≤QFM+1.5.

Results

Whole rock compositions

The sample from the 1937 eruption used in this study is an andesitic pumice, with 62.9 wt% SiO_2, 16.7 wt% Al_2O_3, 2.1 wt% MgO and 5.8 wt% CaO (Fig. 2). Overall, the products from the 1937 eruption span a compositional range from basaltic andesite to dacitic. The two samples with the lowest SiO_2 content (49.8–50.4 wt%) are basaltic enclaves. (Patia, 2004, Patia *et al.*, 2017).

The four lava samples and one volcanic bomb from the 1994 eruption are all andesitic. Most other products of the 1994 eruption are more evolved, with SiO_2 contents of 60.1 to 65.7 wt% (Fig. 2). These five samples have 58.5–61.4 wt% SiO_2, 15.6–16.1 wt% Al_2O_3, 2.2–3.2 wt% MgO and 5.1–6.7 wt% CaO.

The two analysed volcanic bombs from the 2014 eruption are classified as basaltic andesites (Fig. 2). Sample VB_IA contains 56.3 wt% SiO_2, 8.0 wt% CaO, and 4.2 wt% MgO, while sample VB_IB contains 56.9 wt% SiO_2, 7.9 wt% CaO, and 4.0 wt% MgO. These compositions place them among the more primitive products from the 2014 event, which range from basaltic andesite to dacite (Fabbro *et al.*, 2020).

Petrography and mineral assemblage

All samples have porphyritic textures comprising a brown, fine-grained matrix containing microcrystalline plagioclase and pyroxene interspersed throughout with interstitial glass (Supplementary Figs. S3–S6). The bulk mineral assemblage (Table 2) consists of plagioclase, clinopyroxene, orthopyroxene, olivine and Ti-magnetite with accessory apatite and sulfides (Fig. 11). The principal exception is that pumice from the 1937 Rabaul eruption does not contain olivine.

Macrocrysts

Plagioclase

Plagioclase macrocrysts are more abundant than pyroxene or olivine macrocrysts in every sample (Table 2). Plagioclase crystals are hypidiomorphic to idiomorphic and their size ranges from 360×200 μm to 1.4×0.6 mm. Plagioclase crystals plot on the albite-anorthite axis in the plagioclase classification diagram (Supplementary Fig. S7), with compositional ranges of 8.6–21.2 wt% CaO, 0.2–6.3 wt% Na_2O, and 0.0–0.5 wt% K_2O. The anorthite content (An = molar $CaO/(CaO+Na_2O+K_2O)$) in plagioclase crystals varies from 60 mol% to 95 mol%.

Plagioclase crystals in the Rabaul eruption products can be divided into three groups based on their texture and mineral chemistry (Fig. 3). Group one plagioclase crystals have cores of $An_{91\text{-}97}$ (~An_{93} is most common, Fig. 3a), which are resorbed around the edges, and rims of $An_{<75}$ (~An_{69} most common, Figs. 3a–b, 4a–b). Rims of group one cores sometimes feature faint oscillatory zoning (Fig. 3a). Group two plagioclase crystals show patchy zoning with heavily resorbed cores of $An_{80\text{-}89}$ and the same rim compositions as group one (Fig. 3b–c). Group three plagioclase crystals have core compositions below An_{75} with ~An_{69} being the most

common (Fig. 3). The group three plagioclase cores have the same composition as the group one and group two rims. Group three plagioclase crystals can be unzoned or faintly oscillatory zoned with oscillatory zoned crystals spanning from ~An_{64} to ~An_{70} (Fig. 3d, 4c).

The 1937 pumice contains group two and group three plagioclase crystals, while the 1994 and 2014 eruption products contain plagioclase belonging to all three groups (Fig. 3). According to our classification, the 2006 eruption products contain mostly group three and group two plagioclase crystals, only a few group one plagioclase crystals with $An_{>90}$ cores have been reported (Bouvet de Maisonneuve *et al.*, 2015).

Clinopyroxene

Clinopyroxene crystals are typically smaller than plagioclase crystals, hypidiomorphic to idiomorphic, and measure from 110×220 μm to 330×240 μm. Clinopyroxene crystals are diopsidic to augitic in composition (Supplementary Fig. S8), with FeO contents ranging from 4.7 to 16.9 wt%, MgO from 7.4 to 17.3 wt%, and CaO from 12.8 to 23.8 wt%.

Clinopyroxene Mg numbers (Mg# = molar MgO/(MgO+ FeO)) reveal a bimodal distribution of clinopyroxene compositions in the Rabaul samples which we use, along with the mineral textures, to define two groups (Figs. 5, 11). Group one crystals are predominantly Ca-rich diopsides with core compositions of Mg#76–86, most commonly ~Mg#84. These crystals are normally zoned and have rim compositions of Mg#71–77, most commonly ~Mg#75 (Figs. 5a, 6a). Group two clinopyroxene crystals are predominantly augitic, unzoned, and have core compositions of Mg#71–77, most commonly ~Mg#75 (Fig. 5). Rarely, group two clinopyroxene crystals show reverse zoning with core compositions of ~Mg#75, overgrown by alternating bands of high-Mg clinopyroxene with ~Mg#84 and low-Mg clinopyroxene with

~Mg#75 (Fig. 5c–d, 6b). The high-Mg bands in reversely zoned clinopyroxene have a higher Cr_2O_3 concentration (~0.16 wt% on average) than the low-Mg bands (~0.01 wt% on average).

The 1937 pumice only contains group two clinopyroxene crystals, while the 1994 and 2014 samples contain both groups of clinopyroxene (Fig. 5). The 2006 eruption products contain predominantly group two clinopyroxene and some group one clinopyroxene (Bouvet de Maisonneuve *et al.*, 2015).

Orthopyroxene

All the analysed samples carry orthopyroxene, and these crystals show uniform textures and compositions across all our samples (Supplementary Fig. S9). They are typically subhedral to euhedral and generally lack zoning, though some orthopyroxene crystals feature thin, Mg-poor rims (Supplementary Fig. S9). Orthopyroxene contains 16.2–18.3 wt% FeO, 22.5–26.0 wt% MgO, 1.3–3.0 wt% CaO, and 0.5–1.9 wt% Al_2O_3.

Olivine

No olivine was found in the 1937 pumice. Even though olivine was stated to be present in the 2006 eruption products with forsterite (Fo) contents of 69–72 mol% (Fo = molar MgO/(MgO+FeO)) (Bouvet de Maisonneuve *et al.*, 2015), no olivine chemical data were reported for the 2006 eruption products. Olivine crystals in the 1994 and 2014 eruption products are typically subhedral, unzoned and show low-Mg rims (Figs. 7a–b, 8, 11). The modal core composition of olivine crystals is ~Fo_{80} in the 2014 eruption products and ~Fo_{83} in the 1994 products (Fig. 7). The Mg-poor rims around olivine crystals in the 1994 and 2014 samples have compositions of ~$Fo_{65–75}$. Around half of the olivine crystals show variable replacement by orthopyroxene (Fig. 7c–d).

Ti-magnetite

Ti-magnetite is present as small, subhedral to euhedral crystals dispersed in the matrix, attached to other macrocrysts, and as part of mineral clots (Figs. 4c, 5b, 7c, 10c–d). The Ti-magnetite crystals have 43.9–48.4 wt% Fe_2O_3, 35.0–37.7 wt% FeO, and 9.6–11.6 wt% TiO_2. The composition of Ti-magnetite varies slightly between the different eruptions (Fig. 9). The magnetite FeO^T (total iron expressed as FeO) content decreases from an average of 78.4 wt% in the 1937 eruption to an average of 77.9 wt% in the 1994 eruption to an average of 77.4 wt% in the 2014 eruption. In contrast, the TiO_2 and V_2O_3 concentrations in the magnetite increase over time, from the 1937 (~9.7 wt% TiO_2 and ~0.43 wt% V_2O_3) to the 1994 (~10.5 wt% TiO_2 and ~0.48 wt% V_2O_3) to the 2014 eruption (~9.7 wt% TiO_2 and ~0.43 wt% V_2O_3). The Al_2O_3 and MgO concentrations in Ti-magnetite are similar across eruptions within analytical uncertainties (Fig. 9).

Mineral clots

In this study we define mineral clots to be glomerocrystic aggregates of multiple grains, these can be either mono-mineralic or multi-mineralic. Whole thin-section scans illustrate that mineral clots make up <10% of the sample area which is roughly comparable to the abundance of macrocrysts (Figs. S3–S6). The dimension of mineral clots and the number and size of individual crystals within them vary. In the 2014 volcanic bombs, the smallest observed mineral clot found measures 250×300 μm, while the largest measures 5.5×3.8 mm in size. Mineral clots in samples from the 1937, 2006, and 1994 eruptions have similar size ranges.

We distinguish two different types of mineral clots, which we hereafter term ‘mafic’ and ‘intermediate’. Mafic mineral clots consist of variable proportions of group one plagioclase,

group two plagioclase, group one clinopyroxene, olivine and/or minor Ti-magnetite (Figs. 10a–b). Plagioclase is the most abundant phase in the mafic mineral clots followed by clinopyroxene, then olivine. Mafic mineral clots are typically surrounded by small crystals of olivine (~10×30 μm to ~25×25 μm), Ca-rich clinopyroxene (~25×25 μm to ~25×92 μm), and An-rich plagioclase (~10×50 μm to ~15×150 μm) which stand out from the finer-grained crystals and interstitial glass of the matrix. These clusters of small olivine-cpx-plagioclase crystals can also be found in some spots not directly associated with mafic mineral clots (Fig. 10c).

Intermediate mineral clots consists of variable proportions of group two plagioclase, group three plagioclase, group two clinopyroxene, orthopyroxene, and Ti-magnetite (Fig. 11d). Plagioclase is the most abundant phase in the intermediate mineral clots, followed by clinopyroxene, then orthopyroxene. The intermediate mineral clots are not surrounded by olivine, clinopyroxene and plagioclase clusters.

While both types of mineral clots are found in the 1994 and 2014 eruption products, the 1937 pumice only contains intermediate mineral clots. Mineral clots are present in the 2006 eruption products (Bouvet de Maisonneuve *et al.*, 2015), but their study did not distinguish between the different types of mineral clots and not enough textural and chemical information is reported to classify the 2006 mineral clots ourselves. However, both olivine and orthopyroxene are described as being present in mineral clots from the 2006 eruption products (Bouvet de Maisonneuve *et al.*, 2015). Since our study shows that olivine only occurs in mafic mineral clots and orthopyroxene only occurs in intermediate mineral clots, we can infer that both mafic and intermediate mineral clots are present in the 2006 eruption products.

Matrix glass

The 1937 pumice glasses have a very narrow compositional range with 66.5–67.5 wt% SiO_2, 15.1–15.6 wt% Al_2O_3, 4.3–4.9 wt%, 1.1–1.5 wt% MgO and 3.3–3.7 wt% CaO (Fig. 12). They are dacites and their compositions overlap with the 2006 and some of the 1994 matrix glasses.

Matrix glasses in the 1994 eruption products range from basaltic andesites to rhyolites with SiO_2 contents of 53.4 to 78.7 wt% (Fig. 12, Supplementary Figs. S10). These matrix glasses contain 8.3–29.2 wt% Al_2O_3, 0.6–14.5 wt% FeO, up to 5.5 wt% MgO and 0.3–12.9 wt% CaO. Notably, the 1994 matrix glasses segregate into two different trends: samples S152971 (volcanic bomb) and S153127 (lava) have compositions that overlap in their compositions with the 1937 and 2014 glasses, while samples S152972 (lava), S152973 (lava), and S153126 (lava) are characterised by lower MgO, FeO and TiO_2 contents and extend towards higher SiO_2 contents (Fig. S10).

Matrix glasses in the 2006 samples are andesitic to dacitic and have SiO_2 contents between 57.4 and 66.9 wt%. The 2006 matrix glasses record Al_2O_3 contents between 13.7 and 15.5 wt%, FeO of 4.4–10.9 wt%, and CaO between 3.1 and 6.6 wt%. The MgO contents in these glasses are between 1.1 wt% and 3.2 wt% (Bouvet de Maisonneuve *et al.*, 2015).

Matrix glasses in the 2014 volcanic bombs are andesitic and show a narrow compositional range in SiO_2 (58.1–62.3 wt%) but a larger range in MgO between 1.0–5.0 wt%. The matrix glass of the 2014 volcanic bombs varies in Al_2O_3 between 12.8 and 22.4 wt%, with FeO from 3.8–8.7 wt% and CaO between 4.6 and 8.4 wt% (Fig. 12, Supplementary Fig. S10).

We tested for equilibrium between minerals and matrix glass using the K_D values from Putirka (2008) ($K_D(Fe–Mg)^{Ol–liq}$ in the range of 0.30 ±0.03; $K_D(Fe–Mg)^{Cpx–liq}$ in the range of 0.28 ±0.08; $K_D(An\text{-}Ab)^{Pl–liq}$ in the range of 0.27 ±0.11). The majority of the matrix glasses have Mg#30–40 and are in equilibrium with group three plagioclase and group two clinopyroxene cores, and with the low-Mg, low-An, and low-Mg# rims around olivine, group one plagioclase, and group one clinopyroxene (Supplementary Figs. S12–S19). These matrix glasses include all of the 1937 matrix glasses, most of the 2006 and 2014 matrix glasses, and a small group of 1994 matrix glasses (Fig. 12). In contrast, $Fo_{>70}$ olivine, group one clinopyroxene (Mg#>77), and group one and group two plagioclase cores ($An_{>80}$), are not in equilibrium with these abundant matrix glass compositions. These crystals are only in equilibrium with a small subset of matrix glasses that have Mg#>40, and these glass compositions are only be found within ~50 μm of mafic macrocrysts and mafic mineral clots (Supplementary Figs. S12–S19).

Thermobarometry

We conducted cpx-only and cpx-liquid thermobarometry calculations using the models of Jorgenson et al. (2022) and Petrelli et al. (2020) to estimate pressures and temperatures of clinopyroxene crystallisation. Clinopyroxene-liquid calculations yield crystallisation pressures between 0.5 and 4.5 kbar and temperatures between 960 and 1125 °C (Fig. 13). Clinopyroxene-only calculations yield similar temperatures. The output pressures extend up to 6 kbar, but most of the outputs lie between 0.5 and 5 kbar with only a few clinopyroxene crystals in the 2014 eruptions products showing higher pressures (Fig. 14). Our calculations suggest no significant difference in the crystallisation pressures and temperatures of clinopyroxene cores and clinopyroxene rims (Supplementary Figs. S20–23).

Using the Jorgenson et al. (2022) cpx–liquid model, mean pressures cluster around 2.0 ± 0.5 kbar (Supplementary Fig. S24). Although there is minor scatter between eruptions and between group 1 and group 2 crystals, these variations remain within one standard deviation (1σ) and do not reveal any systematic trend. Cpx–only pressures computed with the same model exhibit greater dispersion: group 2 crystals from the 1937 eruption and group 1 crystals from the 1994 and 2014 eruptions average 2.0 ± 0.7 kbar, whereas group 2 crystals from 1994 and 2014 average 1.7 ± 0.5 kbar. Although our overall observations corroborate earlier interpretations that group 1 clinopyroxene crystallized from a more mafic reservoir at greater depth than group 2 clinopyroxene, the mean pressure difference of ~0.3 kbar corresponds to only ~1.2 km in depth and is still encompassed by 1σ uncertainty. The Petrelli et al. (2020) models produce pressures that are ~0.2 kbar higher than those calculated with the Jorgenson et al. (2022) models.

The temperature data further support a modest distinction between clinopyroxene groups. For group 1 clinopyroxene, Jorgenson et al. (2022) cpx–liquid temperatures average 1057 ± 28°C (1994) and 1067 ± 29°C (2014), while cpx–only temperatures average 1072 ± 23°C (1994) and 1060 ± 18°C (2014). Petrelli et al. (2020) yields temperatures within 3°C of these values (Fig. 16). For group 2 clinopyroxene, the Jorgenson model returns cpx–liquid temperatures of 995 ± 6°C (1937), 1045 ± 6°C (1994), and 1056 ± 18°C (2014); cpx–only temperatures are 1035 ± 14°C, 1045 ± 18°C, and 1055 ± 18°C for the same eruptions. Petrelli et al. (2020) produces temperature estimates 9–23°C lower than Jorgenson et al. (2022) for group 2, except for the 1937 eruption, where the cpx–liquid result is 21°C higher. Altogether the slightly elevated temperatures of group 1 clinopyroxene relative to group 2 clinopyroxene remain within 1σ.

In summary, Rabaul clinopyroxene crystallization occurred at pressures of ~2 ± 0.5 kbar (range 0.5–5 kbar) and temperatures of ~1050 ± 50°C (range 960–1 125°C). Fabbro et al. (2020) estimated magma storage conditions for the 2014 eruption products to be between 970–1020°C and 0.4–4 kbar using the two-pyroxene, clinopyroxene-liquid and plagioclase-liquid thermometers and barometers of Putirka (2008). Our P-T results are broadly consistent with these previous estimates. However, Wieser *et al.* (2022) demonstrated that the Putirka (2008) clinopyroxene-liquid barometer underestimates crystallisation pressures for those clinopyroxene crystals in hydrous arc magmas that crystallised deeper than 3 kbar, which could explain the offset with our calculated clinopyroxene pressures of up to 1 kbar. Notably, the Jorgenson et al. (2022) model does not incorporate a water term in the liquid component, thereby reducing one source of uncertainty relative to the Putirka (2008) approach, which requires an explicit water input.

Discussion

Magma storage conditions

Our thermobarometry calculations reveal that group one clinopyroxene records marginally higher pressures (~0.3 kbar) than group two clinopyroxene (Figs. 13, 14). The pressure difference corresponds to a depth offset of approximately 1.2 km. However, the uncertainties on the thermobarometry models are 3.2 kbar and 72.5°C for the cpx-only and 2.7 kbar and 44.9°C for the cpx-liquid models of Jorgenson et al. (2020), and 3 kbar and 40°C for cpx-only and 2.6 kbar and 40°C for the cpx-liquid models of Petrelli et al. (2020). These uncertainties are equivalent to a vertical resolution of ~10–13 km. In fact, (Wieser *et al.*, 2023a) showed that all commonly used thermobarometers can only distinguish magma storage zones that are at least 10–15 km apart. This means that it is challenging to evaluate whether the different

clinopyroxene groups grew under meaningfully different conditions, nor where in the crust those conditions might exist.

Seismic tomography studies have identified two distinct low-velocity zones beneath Rabaul—one at ~0.5–4 km (~0–1.2 kbar) and the other at ~9–15 km (~2.3–3.9 kbar). These observations might be interpreted as evidence for a shallower, felsic and a deeper, mafic magma reservoir. However, the question arises whether thermobarometry outputs should precisely match geophysical observations? Could magmas be crystallising over a wide range of crustal conditions – or indeed over the entire crustal interval? In this scenario, the magma storage beneath Rabaul in the region of ~5–10 km would be in small lenses that are not visible to geophysical imaging techniques. Future work is needed to improve the uncertainty on thermobarometry calculations in order to better resolve the structure of magma plumbing systems underneath arc volcanoes. Advances in geophysical imaging may also provide further insights into cryptic magma storage in the arc crust. Although our thermobarometry results do not fully resolve Rabaul's magma plumbing system architecture given current modelling uncertainties, the mineral chemistries and textures of the erupted crystal cargo preserve clear records of Rabaul's pre-eruptive magma dynamics.

Magmatic processes recorded by the crystal cargo

Mafic mineral clots and the deep basaltic mush

The core compositions of the olivine, group one clinopyroxene, and group one and group two plagioclase crystals found in our mafic mineral clots are not in equilibrium with most majority our matrix glass analyses. This indicates that these mafic crystals did not grow in the magma in which they were erupted but rather represent a crystal cargo inherited from another source,

presumably a magma of lower SiO_2 and higher MgO content. Although the mafic mineral clots we have described likely correspond to the mafic enclaves reported in previous studies (Bouvet de Maisonneuve *et al.*, 2015, Fabbro *et al.*, 2020, Patia *et al.*, 2017), the absence of detailed chemical and textural documentation in these earlier investigations precludes a definitive correlation. Crystals in mafic mineral clots exhibit tightly interlocking euhedral-subhedral boundaries with three-dimensional frameworks and lack a preferred orientation (Fig. 10). We therefore interpret mafic mineral clots as remnants from a deep, basaltic crystal mush reservoir. We suggest that Rabaul's mineral clots can be interpreted as time-capsules that preserve the textural and chemical signatures of their parent primitive mush environment.

The low-An, low-Mg#, and low-Fo rims around group one plagioclase, group one clinopyroxene, and olivine cores (Figs. 3, 5, 7) are in equilibrium with the majority of matrix glasses that have Mg#30–40 and with whole rock compositions (Supplementary Figs. S12–S19). The transition from crystal cores to rims is marked by an abrupt decrease in anorthite content in plagioclase (Fig. 4a) and in Mg# in clinopyroxene (Fig. 6a), without any intermediate compositions. This discrete compositional shift is inconsistent with a continuous fractional crystallization process and instead reflects a sudden change in crystallization conditions (Namur *et al.*, 2020). Comparable rim characteristics have been documented in other volcanic systems undergoing mafic recharge and magma mixing (Coote & Shane, 2016, Namur *et al.*, 2020, Palummo *et al.*, 2021). We therefore interpret these low-An, low-Mg#, and low-Fo rims as overgrowths that formed in equilibrium with a more evolved magma following mixing.

Group one and group two plagioclase crystals share the same low-An ($An_{<75}$) rim compositions. In addition, the cores of both groups are only in equilibrium with the most mafic

matrix glass compositions (Mg#>40, Supplementary Fig. S19). This suggests that both groups of plagioclase have cores that originated in a mafic magma reservoir and subsequently acquired their lower-An rims upon mixing with a more evolved melt. However, group two plagioclase crystals are distinguished by strongly resorbed cores (An_{80-89}) and at times patchy zoning (Fig. 3b–c), in contrast to the little resorbed $An_{91–97}$ cores seen in group one plagioclase crystals (Fig. 3a). These differences imply that group two plagioclase crystals underwent a different magmatic history than group one plagioclase crystals. Decompression induced dissolution during ascent has been proposed to explain resorption textures in plagioclase from other volcanic systems (Coote & Shane, 2016, Streck, 2008, Viccaro *et al.*, 2012). More gradual or stalled ascent in group two plagioclase compared to group one crystals could have led to more extensive resorption of the group two plagioclase crystals. In contrast, group one plagioclase crystals appear to have ascended more rapidly into the shallower, more evolved magma reservoir, acquiring protective felsic overgrowth before significant dissolution could occur (Coote & Shane, 2016, Viccaro *et al.*, 2012).

Magma mixing and crystal transfer

The mafic mineral clots and the mafic macrocrysts formed in a deeper mafic recharge magma and were subsequently transferred into a more evolved magma during magma mixing. Analogous interpretations have been made for other volcanic systems such as for Soufrière Hills volcano and Volcán Quizapu in Chile (Humphreys *et al.*, 2009, Plail *et al.*, 2014, Ruprecht *et al.*, 2012, Ubide *et al.*, 2014). Our observations show that crystals within mafic mineral clots and mafic macrocrysts exhibit identical mineral chemistries and zoning patterns. We suggest that mush formed as crystals settled on the floor of some deep mafic reservoir. This growing mush body was then remobilised, e.g. by melt injection, and this resulted in partial disaggregation forming mafic mineral clots or wholesale disaggregation yielding individual

mafic macrocrysts, both of which were subsequently carried to shallower levels in the plumbing system and, ultimately, erupted. Additionally, the disaggregation of mafic mineral clots can result from the combined effects of partial microlite dissolution, melt flow, and shear forces during magma mixing (Humphreys *et al.*, 2009, Ruprecht *et al.*, 2020).

High thermal contrast between a hot mafic recharge magma and a cooler, more evolved resident magma is known to produce rapid growth textures (Ruprecht *et al.*, 2020). Consistent with this phenomenon, we interpret the fine-grained plagioclase, clinopyroxene, and olivine clusters observed around mafic mineral clots as the same rapid growth textures (Fig. 10), thereby providing further evidence for magma mixing. The same features have been reported in the 2006 Rabaul eruption products (Bouvet de Maisonneuve *et al.*, 2015).

The replacement of olivine macrocrysts by orthopyroxene (Fig. 7c–d) was likely a result of the transfer of these olivine crystals from the deep, mafic mush reservoir, in which they grew, into a more silica-rich (resident) melt during mafic recharge and magma mixing (Coombs & Gardner, 2004, Humphreys *et al.*, 2006, Tsuchiyama, 1986, Zellmer *et al.*, 2016).

Intermediate mineral clots and the shallow andesitic-dacitic mush

Intermediate mineral clots contain group three plagioclase ($An_{<75}$), group three clinopyroxene (Mg#~75), orthopyroxene, and Ti-magnetite. Group three plagioclase core compositions match the rims of both group one and group two plagioclase. Similarly, group two clinopyroxene crystals display chemical compositions identical to the low-Mg# rims around group one clinopyroxene. Moreover, both group three plagioclase crystals and group two clinopyroxene crystals are in equilibrium with matrix glasses with Mg#30–40 and with the whole rock compositions (Supplementary Figs. S15–S19). These observations indicate that, analogous to

the formation of the rims of group one minerals, group three plagioclase and group two clinopyroxene crystallised from the more evolved resident magma in the shallow magma reservoir. Similarly to mafic mineral clots, crystals in intermediate mineral clots exhibit tightly interlocking euhedral-subhedral boundaries with three-dimensional frameworks and lack a preferred orientation (Fig. 10). We therefore interpret intermediate mineral clots to represent cumulate fragments of a second shallower, more evolved crystal mush, likely formed at shallower levels within the magmatic system.

Oscillatory zoning in group three plagioclase likely reflects repeated fluctuations in the magmatic environment during crystal growth (Ginibre *et al.*, 2002, Palummo *et al.*, 2021, Ustunisik *et al.*, 2014). The oscillatory zoning observed in group three plagioclase is characterised by minor fluctuations in anorthite content that remain within the compositional range of group three plagioclase (An_{64}–An_{70}) (Fig. 4c). We attribute these subtle variations to convective movement within a melt-rich magma body that induced periodic changes in temperature, pressure, melt composition and water content (Ginibre *et al.*, 2002, Ustunisik *et al.*, 2014, Viccaro *et al.*, 2012).

Reverse zoning in group two clinopyroxene (Fig. 5c, d) further indicates the occurrence of interaction between a mafic and a more evolved magma. The higher-Mg# bands on these more evolved group two clinopyroxene crystals, commonly referred to as recharge bands (Palummo *et al.*, 2021), suggest that they crystallised in a more mafic liquid relative to the conditions under which the crystal cores formed (Mangler *et al.*, 2022, Palummo *et al.*, 2021). The elevated Cr_2O_3 contents of the Mg#-rich zones corroborate this interpretation, mirroring similar Cr_2O_3 enrichment observed in clinopyroxene from Mt Etna, where mafic recharge leads to the formation of Cr_2O_3-rich zones (Streck, 2008, Ubide & Kamber, 2018). Together, these

observations confirm that the reversely zoned clinopyroxene crystals in the Rabaul eruption products formed as a result of mafic recharge of the reservoir in which the moderate-Mg# cores of group two clinopyroxene had been growing. Additionally, multiple recharge bands in reversely zoned group two clinopyroxene (Fig. 5d) suggests that these crystals underwent multiple episodes of mafic recharge and subsequent magma mixing.

In contrast, neither group three plagioclase nor orthopyroxene exhibit zoning patterns that can be attributed to mafic recharge. Relatively evolved minerals, such as low-An plagioclase and orthopyroxene, are likely concentrated toward the upper regions of the magma reservoir away from the direct influence of mafic recharge. Consequently, these phases remain largely unaffected by the compositional shifts associated with recharge which explains why they do not show recharge related textures.

Summary

Our observations together paint a picture of a vertically extensive, heterogeneous yet interconnected magmatic system beneath Rabaul. Specifically, mafic mineral clots sample deep, basaltic mush, whereas intermediate mineral clots sample a shallower, andesitic-dacitic mush. Mafic recharge pulses ascend from the deep magma reservoir, entraining cumulate fragments and mafic crystals which experience normal-zoned overgrowth following mixing. These episodic mafic injections penetrate the shallow mush, producing reverse-zoned recharge bands around group two clinopyroxene. Both mafic and intermediate mineral clots host group two plagioclase, demonstrating direct physical evidence for interchange between deep and shallow mush levels.

Evidence from magma mixing modelling

We modelled magma mixing in the post-Rabaul Pyroclastics eruption products with a simple, linear, two-endmember mixing model. We define the mafic endmember, interpreted as the recharge magma, as the average composition of the three most mafic samples known from Rabaul which are basaltic enclaves found in the 1878 (sample HPP003a) and 1937 (samples HPP075, HPP075a) eruption products (Cunningham *et al.*, 2009, Patia, 2004). We define the felsic endmember as the average dacitic composition of the Rabaul Pyroclastics eruption products, which represents the last caldera-forming eruption (Fabbro *et al.*, 2020) (Table 3). The calculated mixing line closely matches the whole rock compositional trends displayed by the 1937, 1994, and 2014 Rabaul eruptions (Fig. 15). This correspondence suggests that eruption products could have been formed by mixing a mafic recharge magma with a composition similar to the basaltic Rabaul eruption products, into a magma reservoir of a more evolved magma with a composition similar to the Rabaul Pyroclastics dacites. For the 1994 eruption products that were analysed in this study, the mixing ratios of mafic to dacitic magma range from approximately 3:97 to 20:80, while the 2014 volcanic bombs display a ratio nearer 35:65. In contrast, the 1937 pumice analysed in this study is compositionally akin to the dacitic endmember and contains a negligible proportion of the mafic component (0:100). However, the apparent absence of a mafic component in the 1937 pumice analysed here likely reflects sampling bias: our suite comprises only dacitic pumice, whereas mafic enclaves and other mafic lithologies from the 1937 eruption have been documented (Patia, 2004).

Our modelling results are consistent with our interpretation that the minerals in the post-Rabaul Pyroclastics samples record evidence for mafic recharge into a resident dacitic reservoir. This indicates that all of the post-Rabaul Pyroclastics eruption products are effectively hybrid magmas containing evidence for the interactions of multiple melts and diverse crystal cargos.

Our findings are consistent with previous mixing modelling by Patia et al. (2017) and Fabbro et al. (2020). According to Patia et al. (2017), the 1994 whole rock compositions could have been generated by mixing a basalt with 8–10 wt% MgO, similar to the 1937 basaltic enclaves, with a dacite that has ~1.8 wt% MgO and 64 wt% SiO_2. These compositions are similar to our endmember compositions. Fabbro et al. (2020) also concluded that the post-Rabaul Pyroclastics eruptives could have formed through mixing of a basaltic magma similar in composition to the 1937 basaltic enclaves, with a dacitic magma compositionally similar to the Rabaul Pyroclastics eruptives. In contrast, our results appear to contradict the model proposed by Bouvet de Maisonneuve (2015), who attributed the 2006 eruption products to mixing between a dacitic magma similar to the Rabaul Pyroclastics and a different mafic endmember, a basalt akin to the eruption products of the adjacent mafic stratovolcano Kombiu with a lower MgO content of up to 6.5 wt%. The mafic endmember of our mixing trend is defined by just three samples, and there are no eruptions products with MgO contents between ~5–8 wt% across the entire available Rabaul dataset which means that the mafic endmember of the mixing trajectory is relatively poorly constrained. It is therefore possible that the 1937, 1994, 2006, and 2014 eruptions could have been generated by mixing between a resident dacite and three slightly different mafic endmember recharge magmas. Therefore, further work is needed to better constrain the mafic endmember of the Rabaul magma system.

Oxygen fugacity conditions

Oxygen fugacity has a significant impact on magma differentiation and evolution, both in terms of the chemistry of the melt but also the rheology and, as a result, magma transport dynamics (Cottrell *et al.*, 2021, Kelley & Cottrell, 2009, Kolzenburg *et al.*, 2018). To our knowledge, there are no published measurements of oxygen fugacity conditions for Rabaul magmas. The

only broad statement about likely oxidation state has been made by Bouvet de Maisonneuve *et al.* (2015), who inferred relatively reducing conditions around the nickel-nickel oxide (NNO) oxygen buffer for the Rabaul magma on the grounds that melt inclusions in the 2006 eruption products follow a tholeiitic differentiation trend.

We used the oxybarometer of Arató and Audétat (2017) to calculate the oxygen fugacity for the 1937, 1994 and 2014 eruptions at Rabaul. Our calculations show oxygen fugacity conditions of ΔQFM = +1.3 ±0.02 for the 1937 pumice, ΔQFM = +1.1 ±0.2 for the 1994 volcanic bombs, and ΔQFM = +0.9 ±0.1 for the 2014 volcanic bombs. Our results are in good agreement with oxygen fugacity estimates for global arc magmas, which generally record oxidising conditions around ΔQFM = +1.0 (Cottrell *et al.*, 2021 and references therein). The origin of elevated oxygen fugacity in arc settings has been attributed to an oxidised mantle wedge caused by oxidising slab-derived fluids (Brounce *et al.*, 2014, Cottrell *et al.*, 2021, Kelley & Cottrell, 2009, Kelley & Cottrell, 2012).

However, the oxygen fugacity of arc magmas can also decrease as a result of processes in the magma reservoir such as magnetite crystallisation or sulfur degassing (Kelley & Cottrell, 2012). Early-stage magnetite crystallisation lowers the Fe_2O_3 and FeO^T of the magma, while sulfur degassing causes electron exchanges; both result in a reduction in oxygen fugacity (Jenner *et al.*, 2010, Kelley & Cottrell, 2012). The Rabaul eruption products contain abundant Ti-magnetite. Melt inclusions from the 2014 eruption of Tavurvur show a decrease of TiO_2 starting at ~4 wt% MgO which is when magnetite crystallisation likely commenced. Although fractional crystallization modelling for oxidized (QFM+1) and hydrous (1–6 wt% H_2O) arc magmas support early magnetite crystallization as a potential reducing mechanism (Zimmer *et al.*, 2010), late-stage Ti-magnetite crystallization as observed in the Rabaul magmas has not

been associated with a significant reduction in oxygen fugacity (Kelley & Cottrell, 2012). Thus, we infer that Ti-magnetite crystallization did not drive a significant decrease in oxygen fugacity in these systems and therefore our fO_2 estimates are useful recorders of the redox conditions of the Rabaul magma reservoir.

Conclusions: A revised model for the Rabaul magma plumbing system

We conducted a detailed and systematic investigation of the mineral chemistries and textures of products from the 1937, 1994 and 2014 eruptions at Rabaul. Our findings provide clear evidence that mafic recharge and magma mixing are fundamental processes within the Rabaul magma plumbing system.

Geophysical observations suggest two zones of magma storage underneath Rabaul, at depths of 0.5–4 km and 10–20 km (Bai & Greenhalgh, 2005). Our clinopyroxene-liquid and clinopyroxene-only thermobarometry calculations show that Rabaul clinopyroxene crystallised at pressures of ~2 ± 0.5 kbar (range 0.5–5 kbar, corresponding to 2–20 km based on Rasmussen et al.'s crustal density model) and temperatures of ~1050 ± 50°C (range 960–1 125°C).

The broad spread of PT estimates can arise from analytical and calibrations limitations of existing clinopyroxene-liquid and clinopyroxene-only thermobarometers, which are not yet optimised to resolve crystallisation conditions in hydrous arc magmas with high precision. An alternative explanation is that crystallisation of clinopyroxene occurred over a wide vertical interval from near-surface levels to depths of up to 20 km, implying a complex plumbing system with numerous levels of magma storage and evolution. Consequently, clinopyroxene

thermobarometry by itself cannot uniquely reconstruct the precise depth architecture of the Rabaul system. However, when combined with independent lines of evidence, notably the textural record, distinctive mineral populations, and magma-mixing models, the data remain most consistent with a complex, vertically distributed mush system.

Based on our investigation of the crystal cargo of Rabaul's eruption products, we propose a refined conceptual model for the architecture of the Rabaul magma plumbing system (Fig. 16). Our magma mixing modelling supports a scenario in which crystal fragments and basaltic recharge magma from a deep, mafic mush reservoir are injected into a main dacitic mush reservoir, leading to magma mixing that subsequently generates the andesitic-dacitic compositions of all post-Rabaul Pyroclastics eruption products. Mafic mineral clots, and derived macrocrysts, composed of olivine, high-An (group one) plagioclase, and high-Mg, calcium-rich (group one) clinopyroxene, are pervasive in many post-Rabaul Pyroclastics erupted products, though the relative abundance of these varies and probably exerts a strong influence on the measured range of whole rock compositions. Mafic mineral clots and crystals probably grow in the deeper parts of the plumbing system, accumulating in mushy bodies. These must then be disaggregated and partially remobilised by intruding melts, which then rise to shallower levels of the crust carrying their mafic crystal cargo. On contact with the more felsic magma mixing takes place. The high thermal contrast between hot recharge magma and the cooler resident magma promotes rapid growth of olivine, clinopyroxene, and plagioclase clusters around mafic enclaves (Ruprecht *et al.*, 2020). This chemical and thermal disequilibrium is further manifested by the dissolution around crystal rims. Upon magma mixing, evolved crystal overgrowths form around mafic clinopyroxene, olivine, and plagioclase crystals. The compositions of these evolved overgrowths resemble those of group three plagioclase and group two clinopyroxene, which represent the crystals growing in

equilibrium with the hybrid magmas produced by mixing. Some of these crystals aggregate into a second population of mineral clots, consisting of varying proportions of group three plagioclase, group two clinopyroxene, orthopyroxene, and Ti-magnetite. These intermediate mineral clots represent a second, more evolved mush body at a shallower depth.

Our oxybarometry calculations reveal that the mixed magma records oxidising conditions, with oxygen fugacity values of QFM+0.9 to QFM+1.3. This finding is consistent with the broader global trend that arc magmas typically record oxidising conditions around ΔQFM+1.0 (Cottrell *et al.*, 2021 and references therein).

In summary, our study establishes that repeated episodes of mafic recharge and subsequent magma mixing are critical processes in the evolution of the Rabaul magma plumbing system. Our refined conceptual model, supported by integrated geophysical, geochemical, and thermobarometric data, highlights a complex, multi-layered magma storage system with a heterogeneous but interconnected mush reservoir.

Acknowledgements

We thank Ben Ellis and Jasper Berndt-Gerdes for important help with XRF and electron microprobe analyses.

Data availability

Data underlying this article are available in the article and its online supplementary material as well as in the GFZ Data Services data repository, at https://dx.doi.org/ [doi].

References

Anderson, A. T. (1976). Magma mixing: petrological process and volcanological tool. *Journal of Volcanology and Geothermal Research* **1**, 3-33.

Annen, C., Blundy, J. D. & Sparks, R. S. J. (2006). The Genesis of Intermediate and Silicic Magmas in Deep Crustal Hot Zones. *Journal of Petrology* **47**, 505-539.

Arató, R. & Audétat, A. (2017). FeTiMM – A new oxybarometer for mafic to felsic magmas. *Geochemical Perspectives Letters*, 19-23.

Bai, C.-y. & Greenhalgh, S. (2005). 3D multi-step travel time tomography: Imaging the local, deep velocity structure of Rabaul volcano, Papua New Guinea. *Physics of the Earth and Planetary Interiors* **151**, 259-275.

Baldwin, S. L., Fitzgerald, P. G. & Webb, L. E. (2012). Tectonics of the New Guinea Region. *Annual Review of Earth and Planetary Sciences* **40**, 495-520.

Bernard, O. & Bouvet de Maisonneuve, C. (2020). Controls on eruption style at Rabaul, Papua New Guinea – Insights from microlites, porosity and permeability measurements. *Journal of Volcanology and Geothermal Research* **406**.

Bouvet de Maisonneuve, C., Costa, F., Patia, H. & Huber, C. (2015). Mafic magma replenishment, unrest and eruption in a caldera setting: insights from the 2006 eruption of Rabaul (Papua New Guinea). *Geological Society, London, Special Publications* **422**, 17-39.

Brounce, M. N., Kelley, K. A. & Cottrell, E. (2014). Variations in $Fe^{3+}/\sum Fe$ of Mariana Arc Basalts and Mantle Wedge fO_2. *Journal of Petrology* **55**, 2513-2536.

Cashman, K. V. & Sparks, R. S. J. (2013). How volcanoes work: A 25 year perspective. *Geological Society of America Bulletin* **125**, 664-690.

Coombs, M. L. & Gardner, J. E. (2004). Reaction rim growth on olivine in silicic melts: Implications for magma mixing. *American Mineralogist* **89**, 748-758.

Coote, A. C. & Shane, P. (2016). Crystal origins and magmatic system beneath Ngauruhoe volcano (New Zealand) revealed by plagioclase textures and compositions. *Lithos* **260**, 107-119.

Cottrell, E., Birner, S. K., Brounce, M., Davis, F. A., Waters, L. E. & Kelley, K. A. (2021). Oxygen Fugacity Across Tectonic Settings. In: Moretti, R. & Neuville, D. R. (eds.) *Magma Redox Geochemistry*, 33-61.

Cunningham, H. S., Turner, S. P., Dosseto, A., Patia, H., Eggins, S. M. & Arculus, R. J. (2009). Temporal Variations in U-series Disequilibria in an Active Caldera, Rabaul, Papua New Guinea. *Journal of Petrology* **50**, 507-529.

Delph, J. R., Ward, K. M., Zandt, G., Ducea, M. N. & Beck, S. L. (2017). Imaging a magma plumbing system from MASH zone to magma reservoir. *Earth and Planetary Science Letters* **457**, 313-324.

Edmonds, M., Cashman, K. V., Holness, M. & Jackson, M. (2019). Architecture and dynamics of magma reservoirs. *Philosophical Transactions of the Royal Society A: Mathematical, Physical and Engineering Sciences* **377**, 20180298.

Fabbro, G. N., McKee, C. O., Sindang, M. E., Eggins, S. M. & Bouvet de Maisonneuve, C. (2020). Variable mafic recharge across a caldera cycle at Rabaul, Papua New Guinea. *Journal of Volcanology and Geothermal Research* **393**.

Fearnley, C. J., Bird, D. K., Haynes, K., McGuire, W. J. & Jolly, G. (2018). *Observing the Volcano World*: Springer.

Finlayson, D. M., Gudmundsson, O., Itikarai, I., Nishimura, Y. & Shimamura, H. (2003). Rabaul volcano, Papua New Guinea: seismic tomographic imaging of an active caldera. *Journal of Volcanology and Geothermal Research* **124**, 153-171.

Ginibre, C., Kronz, A. & Wörner, G. (2002). High-resolution quantitative imaging of plagioclase composition using accumulated backscattered electron images: new constraints on oscillatory zoning. *Contributions to Mineralogy and Petrology* **142**, 436-448.

Global Volcanism Program. (1994a). Report on Rabaul (Papua New Guinea) (Venzke, E., ed.). *Bulletin of the Global Volcanism Network, 19:9*: Smithsonian Institution.

Global Volcanism Program. (1994b). Report on Rabaul (Papua New Guinea) (Wunderman, R., ed.). *Bulletin of the Global Volcanism Network, 19:10*: Smithsonian Institution.

Global Volcanism Program. (2006). Report on Rabaul (Papua New Guinea) (Wunderman, R., ed.). *Bulletin of the Global Volcanism Network, 31:9*: Smithsonian Institution.

Global Volcanism Program. (2007). Report on Rabaul (Papua New Guinea) (Wunderman, R., ed.). *Bulletin of the Global Volcanism Network, 32:6*: Smithsonian Institution.

Global Volcanism Program. (2011). Report on Rabaul (Papua New Guinea) (Wunderman, R., ed.). *Bulletin of the Global Volcanism Network, 36:7*: Smithsonian Institution.

Global Volcanism Program. (2013). Report on Rabaul (Papua New Guinea) (Wunderman, R., ed.). *Bulletin of the Global Volcanism Network, 38.10*: Smithsonian Institution.

Global Volcanism Program. (2017). Report on Rabaul (Papua New Guinea) (Crafford, A.E., and Venzke, E., eds.). *Bulletin of the Global Volcanism Network, 42:2*: Smithsonian Institution.

Global Volcanism Program. (2021). Report on Rabaul (Papua New Guinea) (Sennert, S., ed.). *Weekly Volcanic Activity Report, 13 October–19 October 2021*: Smithsonian Institution and US Geological Survey.

Global Volcanism Program. (2024). Report on Rabaul (Papua New Guinea) (Senner, S., ed.). *Weekly Volcanic Activity Report, 30 October–5 November 2024*: Smithsonian Institution and US Geological Survey.

Grove, T., Parman, S., Bowring, S., Price, R. & Baker, M. (2002). The role of an H_2O-rich fluid component in the generation of primitive basaltic andesites and andesites from the Mt. Shasta region, N California. *Contributions to Mineralogy and Petrology* **142**, 375-396.

Heming, R. F. (1974). Geology and Petrology of Rabaul Caldera, Papua New Guinea. *Geological Society of America Bulletin* **85**, 1253–1264.

Heming, R. F. (1977). Mineralogy and proposed P-T paths of basaltic lavas from Rabaul caldera, Papua New Guinea. *Contributions to Mineralogy and Petrology* **61**, 15–33.

Hildreth, W. & Moorbath, S. (1988). Crustal contributions to arc magmatism in the Andes of Central Chile. *Contributions to Mineralogy and Petrology* **98**, 455-489.

Hohl, S. V., Schuth, S., Münker, C., König, S., Garbe-Schönberg, D. & Kuduon, J. (2022). Geochemical evolution of the Rabaul volcanic complex, Papua New Guinea – Insights from HFSE, Sr-Nd-Hf, and Fe isotopes. *Lithos* **408-409**.

Holm, R. J., Rosenbaum, G. & Richards, S. W. (2016). Post 8 Ma reconstruction of Papua New Guinea and Solomon Islands: Microplate tectonics in a convergent plate boundary setting. *Earth-Science Reviews* **156**, 66–81.

Horn, E. L., Taylor, R. N., Gernon, T. M., Stock, M. J. & Farley, E. M. R. (2022). Composition and Petrology of a Mush-Bearing Magma Reservoir beneath Tenerife. *Journal of Petrology* **63**.

Humphreys, M. C. S., Blundy, J. D. & Sparks, R. S. J. (2006). Magma Evolution and Open-System Processes at Shiveluch Volcano: Insights from Phenocryst Zoning. *Journal of Petrology* **47**, 2303-2334.

Humphreys, M. C. S., Christopher, T. & Hards, V. (2009). Microlite transfer by disaggregation of mafic inclusions following magma mixing at Soufrière Hills volcano, Montserrat. *Contributions to Mineralogy and Petrology* **157**, 609-624.

Itikarai, I. (2008). The 3-D structure and earthquake locations at Rabaul Caldera, Papua New Guinea. *The Australian National University*.

Jenner, F. E., O'Neill, H. S. T. C., Arculus, R. J. & Mavrogenes, J. A. (2010). The Magnetite Crisis in the Evolution of Arc-related Magmas and the Initial Concentration of Au, Ag and Cu. *Journal of Petrology* **51**, 2445-2464.

Johnson, R. W. (2013a). Eruptions at Rabaul: 1994–1999. *Fire Mountains of the Islands: A History of Volcanic Eruptions and Disaster Management in Papua New Guinea and the Solomon Islands*: ANU Press.

Johnson, R. W. (2013b). *Fire Mountains of the Islands: A History of Volcanic Eruptions and Disaster Management in Papua New Guinea and the Solomon Islands*: ANU Press.

Jorgenson, C., Higgins, O., Petrelli, M., Begue, F. & Caricchi, L. (2022). A Machine Learning-Based Approach to Clinopyroxene Thermobarometry: Model Optimization and Distribution for Use in Earth Sciences. *Journal of Geological Research: Solid Earth* **127**, e2021JB022904.

Kelley, K. A. & Cottrell, E. (2009). Water and the oxidation state of subduction zone magmas. *Science* **325**, 605-607.

Kelley, K. A. & Cottrell, E. (2012). The influence of magmatic differentiation on the oxidation state of Fe in a basaltic arc magma. *Earth and Planetary Science Letters* **329-330**, 109-121.

Kolzenburg, S., Di Genova, D., Giordano, D., Hess, K. U. & Dingwell, D. B. (2018). The effect of oxygen fugacity on the rheological evolution of crystallizing basaltic melts. *Earth and Planetary Science Letters* **487**, 21-32.

Lanari, P., Markmann, T., Laughton, J. & Tedeschi, M. (2023). XMapTools 4.2. Zenodo.

Mangler, M. F., Petrone, C. M. & Prytulak, J. (2022). Magma recharge patterns control eruption styles and magnitudes at Popocatépetl volcano (Mexico). *Geology* **50**, 366-370.

Mason, P. R. D., Downes, H., Thirlwall, M. F., Seghedi, I., SzakÁCs, A., Lowry, D. & Mattey, D. (1996). Crustal Assimilation as a Major Petrogenetic Process in the East Carpathian Neogene and Quaternary Continental Margin Arc, Romania. *Journal of Petrology* **37**, 927-959.

McKee, C. O., Baillie, M. G. & Reimer, P. J. (2015). A revised age of ad 667–699 for the latest major eruption at Rabaul. *Bulletin of Volcanology* **77**.

McKee, C. O. & Duncan, R. A. (2016). Early volcanic history of the Rabaul area. *Bulletin of Volcanology* **78**.

McKee, C. O., Lowenstein, P. L., Saint Ours, P., Talai, B., Itikarai, I. & Mori, J. J. (1984). Seismic and ground deformation crises at Rabaul Caldera: Prelude to an eruption? *Bulletin Volcanologique* **47**, 397-411.

Morgavi, D., Laumonier, M., Petrelli, M. & Dingwell, D. B. (2022). Decrypting Magma Mixing in Igneous Systems. *Reviews in Mineralogy and Geochemistry* **87**, 607-638.

Mori, J. & McKee, C. (1987). Outward-dipping ring-fault structure at rabaul caldera as shown by earthquake locations. *Science* **235**, 193-195.

Nairn, I. A., McKee, C. O., Talai, B. & Wood, C. P. (1995). Geology and eruptive history of the Rabaul Caldera area, Papua New Guinea. *Journal of Volcanology and Geothermal Research* **69**, 255–284.

Nairn, I. A., Wood, C. P., Talai, B. & Mckee, C. O. (1989). Rabaul Caldera, Papua New Guinea—125,000 reconnaissance Geological Map and Eruption History. New Zealand Geological Survey.

Namur, O., Montalbano, S., Bolle, O. & Vander Auwera, J. (2020). Petrology of the April 2015 Eruption of Calbuco Volcano, Southern Chile. *Journal of Petrology* **61**.

Neave, D. A., Bali, E., Guðfinnsson, G. H., Halldórsson, S. A., Kahl, M., Schmidt, A.-S. & Holtz, F. (2019). Clinopyroxene–Liquid Equilibria and Geothermobarometry in Natural and Experimental Tholeiites: the 2014–2015 Holuhraun Eruption, Iceland. *Journal of Petrology* **60**, 1653-1680.

Neave, D. A., Stewart, A., Hartley, M. E. & Namur, O. (2024). Iron valence systematics in clinopyroxene crystals from ocean island basalts. *Contributions to Mineralogy and Petrology* **179**.

Palummo, F., Mollo, S., Petrone, C. M., Ellis, B. S., De Astis, G., Nazzari, M., Scarlato, P. & Bachmann, O. (2021). Decoding multiple zoning patterns in clinopyroxene phenocrysts at Vulcano Island: A record of dynamic crystallization through interconnected reservoirs. *Lithos*

406-407.

Patia, H. (2004). Petrology and geochemistry of the recent eruption history at Rabaul Caldera. *University of Papua New Guinea, Port Moresby*.

Patia, H., Eggins, S. M., Arculus, R. J., McKee, C. O., Johnson, R. W. & Bradney, A. (2017). The 1994–2001 eruptive period at Rabaul, Papua New Guinea: Petrological and geochemical evidence for basalt injections into a shallow dacite magma reservoir, and significant SO_2 flux. *Journal of Volcanology and Geothermal Research* **345**, 200–217.

Paulatto, M., Moorkamp, M., Hautmann, S., Hooft, E., Morgan, J. V. & Sparks, R. S. J. (2019). Vertically Extensive Magma Reservoir Revealed From Joint Inversion and Quantitative Interpretation of Seismic and Gravity Data. *Journal of Geophysical Research: Solid Earth* **124**, 11170-11191.

Petrelli, M., Caricchi, L. & Perugini, D. (2020). Machine Learning Thermo-Barometry: Application to Clinopyroxene-Bearing Magmas. *Journal of Geophysical Research: Solid Earth* **125**.

Plail, M., Barclay, J., Humphreys, M. C. S., Edmonds, M., Herd, R. A. & Christopher, T. E. (2014). Chapter 18 Characterization of mafic enclaves in the erupted products of Soufrière Hills Volcano, Montserrat, 2009 to 2010. *Geological Society, London, Memoirs* **39**, 343-360.

Putirka, K. D. (2008). Thermometers and Barometers for Volcanic Systems. *Reviews in Mineralogy and Geochemistry* **69**, 61-120.

Rasmussen, D. J., Plank, T. A., Roman, D. C. & Zimmer, M. M. (2022). Magmatic water content controls the pre-eruptive depth of arc magmas. *Science* **375**, 1169-1172.

Reubi, O. & Blundy, J. (2009). A dearth of intermediate melts at subduction zone volcanoes and the petrogenesis of arc andesites. *Nature* **461**, 1269-1273.

Roggensack, Williams, Schaefer & Parnell. (1996). Volatiles from the 1994 Eruptions of Rabaul: Understanding Large Caldera Systems. *Science* **273**, 490–493.

Ruprecht, P., Bergantz, G. W., Cooper, K. M. & Hildreth, W. (2012). The Crustal Magma Storage System of Volcán Quizapu, Chile, and the Effects of Magma Mixing on Magma Diversity. *Journal of Petrology* **53**, 801-840.

Ruprecht, P., Simon, A. C. & Fiege, A. (2020). The Survival of Mafic Magmatic Enclaves and the Timing of Magma Recharge. *Geophysical Research Letters* **47**.

Saunders, S., Tenor, E., Wakawa, J. & Nohou, J. (2023). Twenty-Two Years of GPS Monitoring at Rabaul Caldera, a Narrative History. *Geosciences* **13**.

Saunders, S. J. (2001). The shallow plumbing system of Rabaul caldera: a partially intruded ring fault? *Bulletin of Volcanology* **63**, 406-420.

Sparks, R. S. J., Annen, C., Blundy, J. D., Cashman, K. V., Rust, A. C. & Jackson, M. D. (2019). Formation and dynamics of magma reservoirs. *Philosophical Transactions of the Royal Society A: Mathematical, Physical and Engineering Sciences* **377**, 20180019.

Sparks, R. S. J. & Marshall, L. A. (1986). Thermal and mechanical constraints on mixing between mafic and silicic magmas. *Journal of Volcanology and Geothermal Research* **29**, 99-124.

Sparks, S. R. J., Sigurdsson, H. & Wilson, L. (1977). Magma mixing: a mechanism for triggering acid explosive eruptions. *Nature* **267**, 315-318.

Streck, M. J. (2008). Mineral Textures and Zoning as Evidence for Open System Processes. *Reviews in Mineralogy and Geochemistry* **69**, 595-622.

Takach, M. K., Tepley, F. J., Harpel, C. J., Aguilar, R. & Rivera, M. (2024). To Mix or Not to Mix: Details of Magma Storage, Recharge, and Remobilization during the Pacheco Stage at Misti Volcano, Peru (≤21–2 ka). *Journal of Petrology* **65**.

Tsuchiyama, A. (1986). Experimental study of olivine-melt reaction and its petrological implications. *Journal of Volcanology and Geothermal Research* **29**, 245-264.

Ubide, T., Galé, C., Larrea, P., Arranz, E., Lago, M. & Tierz, P. (2014). The Relevance of Crystal Transfer to Magma Mixing: a Case Study in Composite Dykes from the Central Pyrenees. *Journal of Petrology* **55**, 1535-1559.

Ubide, T. & Kamber, B. S. (2018). Volcanic crystals as time capsules of eruption history. *Nature communications* **9**, 326.

Ubide, T., Neave, D. A., Petrelli, M. & Longpré, M.-A. (2021). Editorial: Crystal Archives of Magmatic Processes. *Frontiers in Earth Science* **9**.

Ustunisik, G., Kilinc, A. & Nielsen, R. L. (2014). New insights into the processes controlling compositional zoning in plagioclase. *Lithos* **200-201**, 80-93.

Viccaro, M., Giuffrida, M., Nicotra, E. & Ozerov, A. Y. (2012). Magma storage, ascent and recharge history prior to the 1991 eruption at Avachinsky Volcano, Kamchatka, Russia: Inferences on the plumbing system geometry. *Lithos* **140-141**, 11-24.

Wieser, P., Kent, A. & Till, C. (2023a). Barometer behaving badly II: A critical evaluation of Cpx-only and Cpx-liq thermobarometry in variably-hydrous arc magmas.

Wieser, P., Petrelli, M., Lubbers, J., Wieser, E., Ozaydin, S., Kent, A. & Till, C. (2022). Thermobar: An open-source Python3 tool for thermobarometry and hygrometry. *Volcanica* **5**, 349-384.

Wieser, P. E., Kent, A. J. R., Till, C. B., Donovan, J., Neave, D. A., Blatter, D. L. & Krawczynski, M. J. (2023b). Barometers Behaving Badly I: Assessing the Influence of Analytical and Experimental Uncertainty on Clinopyroxene Thermobarometry Calculations at Crustal Conditions. *Journal of Petrology* **64**.

Wood, C. P., Nairn, I. A., Mckee, C. O. & Talai, B. (1995). Petrology of the Rabaul Caldera area, Papua New Guinea. *Journal of Volcanology and Geothermal Research* **69**, 285–302.

Zellmer, G. F., Sakamoto, N., Matsuda, N., Iizuka, Y., Moebis, A. & Yurimoto, H. (2016). On progress and rate of the peritectic reaction Fo + SiO_2 → En in natural andesitic arc magmas. *Geochimica et Cosmochimica Acta* **185**, 383-393.

Zimmer, M. M., Plank, T., Hauri, E. H., Yogodzinski, G. M., Stelling, P., Larsen, J., Singer, B., Jicha, B., Mandeville, C. & Nye, C. J. (2010). The Role of Water in Generating the Calc-alkaline Trend: New Volatile Data for Aleutian Magmas and a New Tholeiitic Index. *Journal of Petrology* **51**, 2411-2444.

Table 1: Recent eruption history of Rabaul (modified after Fabbro *et al.*, 2020, Nairn *et al.*, 1995, Patia *et al.*, 2017).

date/age (CE)	source of eruption	description	volume (km^3)	VEI
2014	Tavurvur	Strombolian activity with lava flows in the beginning, then change to vulcanian eruption style	?	3
2006	Tavurvur	Sub-Plinian eruption with ash fall, debris flow from partial collapse of northwest flank, change to strombolian style with lava effusion	0.2	4
1994	Vulcan and Tavurvur	Plinian eruption at Vulcan with intra-caldera pyroclastic flows and ash fall; strombolian eruption at Tavurvur with lava flow	V: 0.26 T: 0.04	4
1937–1943	Vulcan and Tavurvur	Sub-Plinian eruption at Vulcan including interaction with seawater; discrete vulcanian event at Tavurvur	0.005	4
1878	Vulcan and Tavurvur	Submarine, pyroclastic cone-building eruption at Vulcan; strombolian and vulcanian activity at Tavurvur	V: 0.3 T: 0.05	3
1791	Tavurvur	Lava and pyroclastic eruptions	?	2
1767	Rabalanakaia or Tavurvur	Lava and pyroclastic eruptions	?	2

Table 2: Samples analysed in this study. Modal mineralogy is calculated on a vesicle-free basis.

Eruption	Vent	Sample Location	Sample	Rock Type	Vesicles (vol%)	Cryst.	Mineral Assemblage (Vol%)					
							gl	plg	cpx	opx	ol	mgt
1937	Vulcan	004.27253 S, 152.16901 E	RBL_1937_pum	pumice	80–85	0.15	85	13	1.0	0.5		0.5
	Tavurvur	flanks	S152971	volcanic bomb	58	0.3	70	20	7.0	1.5	0.5	1.0
	Tavurvur	flanks	S152972	lava	19	0.36	64	25	4.0	3.0	2.0	2.0
1994	Tavurvur	flanks	S152973	lava	7	0.25	75	18	4.0	1.0	1.0	1.0
	Tavurvur	flanks	S153126	lava	4	0.39	61	27	7.0	2.0	2.0	1.0
	Vulcan	flanks	S153127	lava	17	0.29	71	23	3.0	2.0	<0.1	1.0
2014	Tavurvur	4S 13.815', 152E, 12.205'	VB_IA*	volcanic bomb								
2014	Tavurvur	4S 13.815', 152E, 12.205'	VB_IB	volcanic bomb	61	0.38	62	28	6.5	2.0	1.0	0.5

Table 3: Mafic and felsic compositions used for magma mixing modelling. The mafic endmember is the average composition of the most mafic samples known from Rabaul (Cunningham *et al.*, 2009, Patia, 2004). The felsic endmember is a dacite from the Rabaul Pyroclastics eruption (Fabbro *et al.*, 2020).

	SiO_2	TiO_2	Al_2O_3	Fe_2O_3	MnO	MgO	CaO	Na_2O	K_2O	P_2O_5	Total
mafic comp.	50.6	0.8	15.7	10.0	0.2	8.1	12.0	2.3	0.8	0.2	100.6
felsic comp.	62.5	0.9	15.6	6.6	0.2	2.0	4.9	4.5	2.5	0.3	100.0

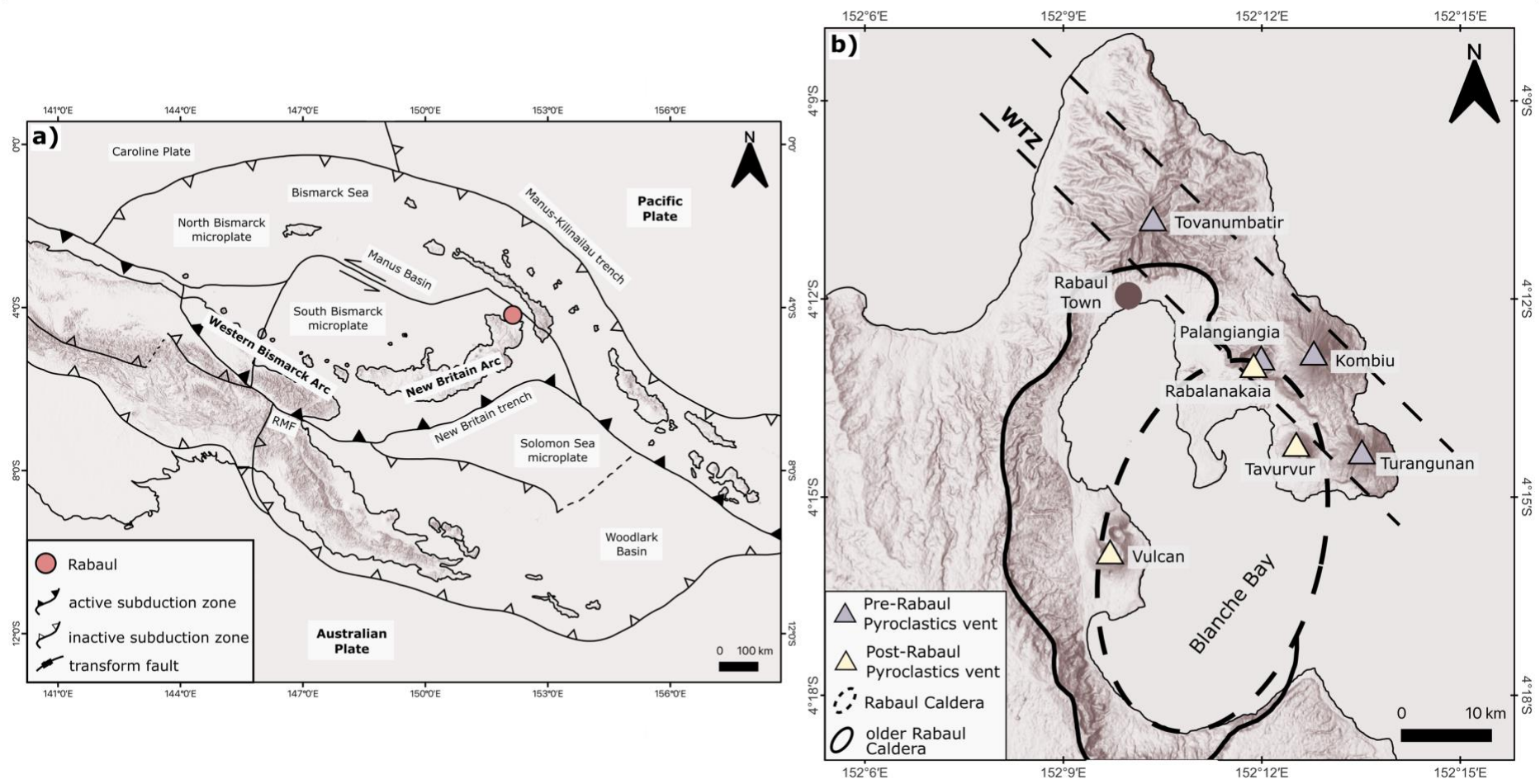

Figure 1: a) Tectonic setting of New Britain Island (tectonic elements after Holm et al., 2019; topographic map: Esri World Topo Map). RMF = Ramu-Marham fault. **b)** Overview of the Rabaul Caldera Complex (vent and caldera locations after Fabbro et al., 2020; topographic map: Esri World Topo Map). WTZ = Watom-Turangunan-Zone.

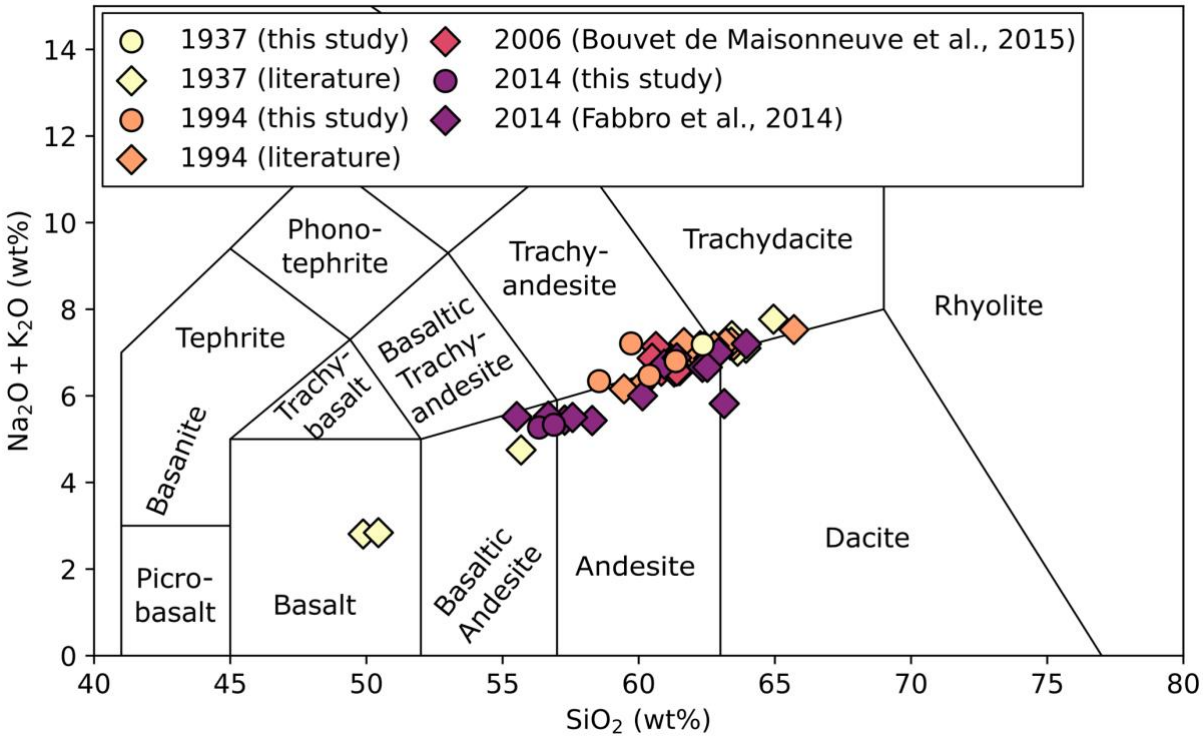

Figure 2: TAS diagrams comparing whole rock compositions of samples analysed in this study for eruptions from the years **a)** 1937 and 1994 and **b)** 2014 with literature data for the post-Rabaul Pyroclastics eruptions (literature data from Bernard & Bouvet de Maisonneuve, 2020, Bouvet de Maisonneuve *et al.*, 2015, Cunningham *et al.*, 2009, Fabbro *et al.*, 2020, Heming, 1974, Hohl *et al.*, 2022, Nairn *et al.*, 1989, Patia, 2004, Patia *et al.*, 2017).

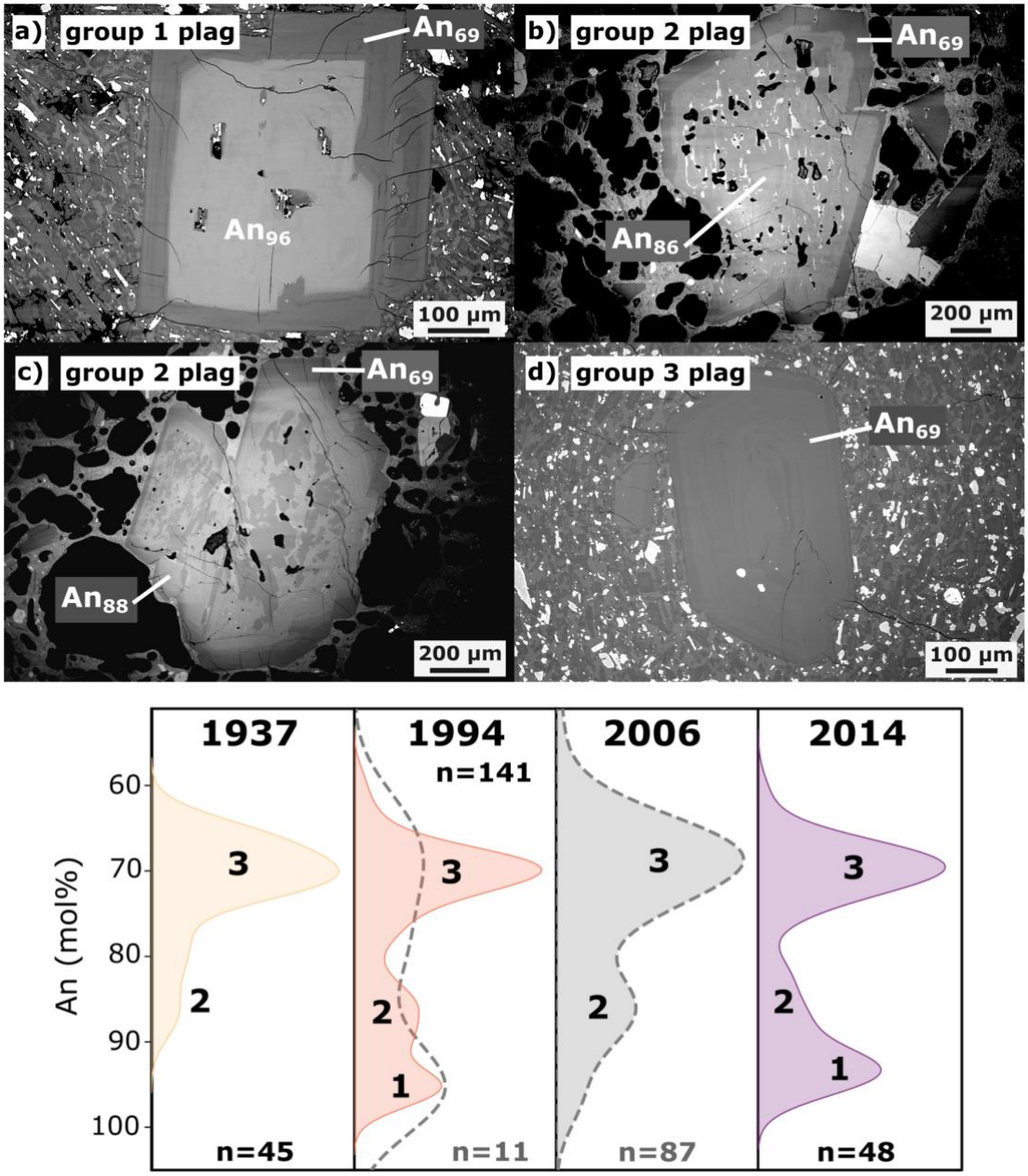

Figure 3: **Upper:** Backscattered electron images showing **a)** group one plagioclase with An-rich core and An-poorer rim, **b)** group two plagioclase with An-rich core and patchy zones of lower An composition, **c)** group two plagioclase with An-rich, resorbed core and An-poorer rim, **d)** group three plagioclase with faint oscillatory zoning. All images are of products from the 1994 eruption. **Lower:** Frequency plots showing the distribution of plagioclase core compositions for the different eruptions of Rabaul. The numbers mark the peaks of group one, group two, and group three plagioclase core compositions. Coloured shaded curves are data from this study; grey dotted curves are literature data. (Bouvet de Maisonneuve *et al.*, 2015, Cunningham *et al.*, 2009, Patia, 2004). Number of analyses are given in black (this study) and grey (literature data).

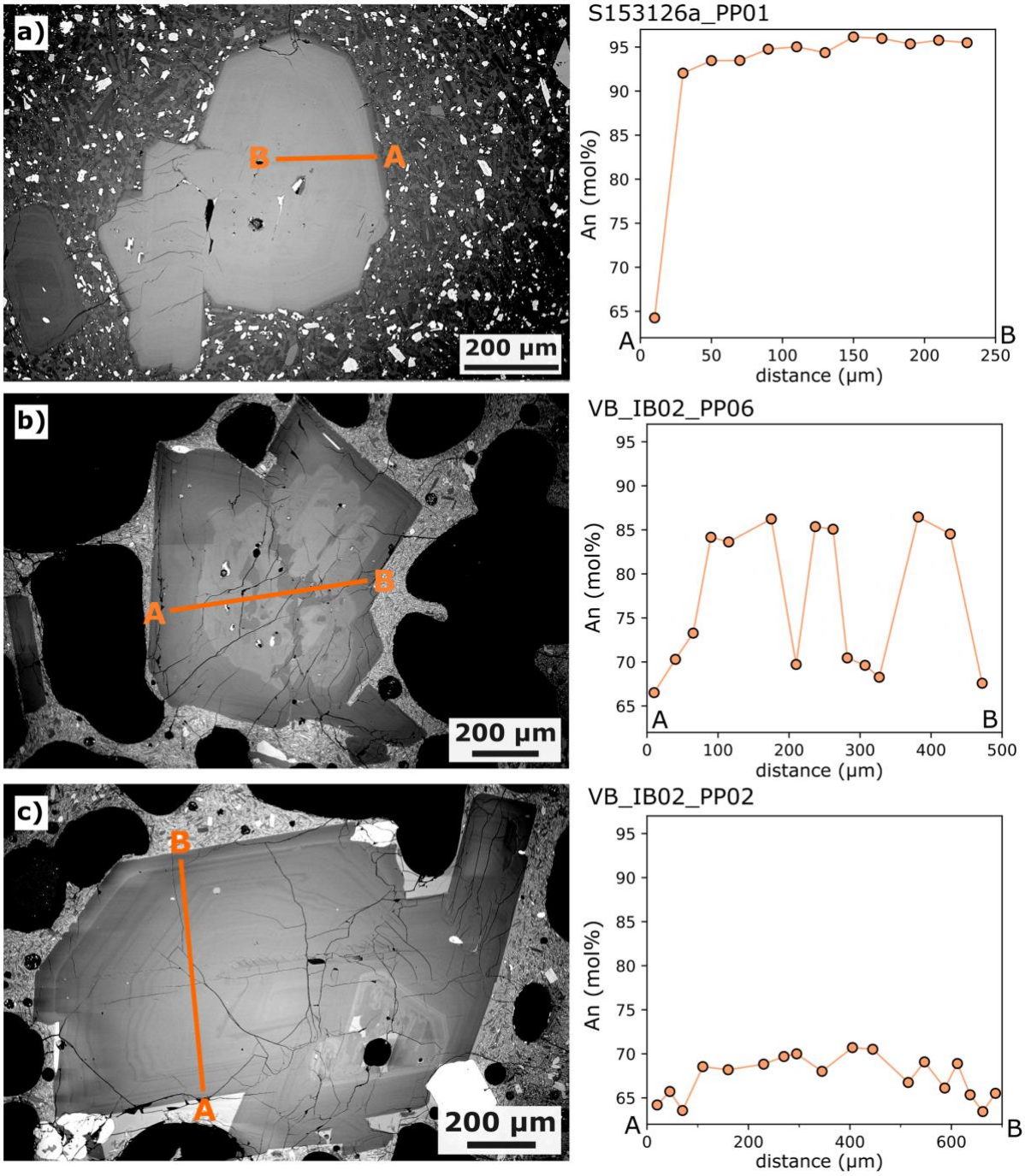

Figure 4: Examples of compositional zoning profiles in **a)** group one plagioclase from the 1994 Rabaul eruption, **b)** group two plagioclase from the 2014 Rabaul eruption, **c)** group three plagioclase from the 2014 Rabaul eruption. Orange lines across crystals mark the locations of profiles.

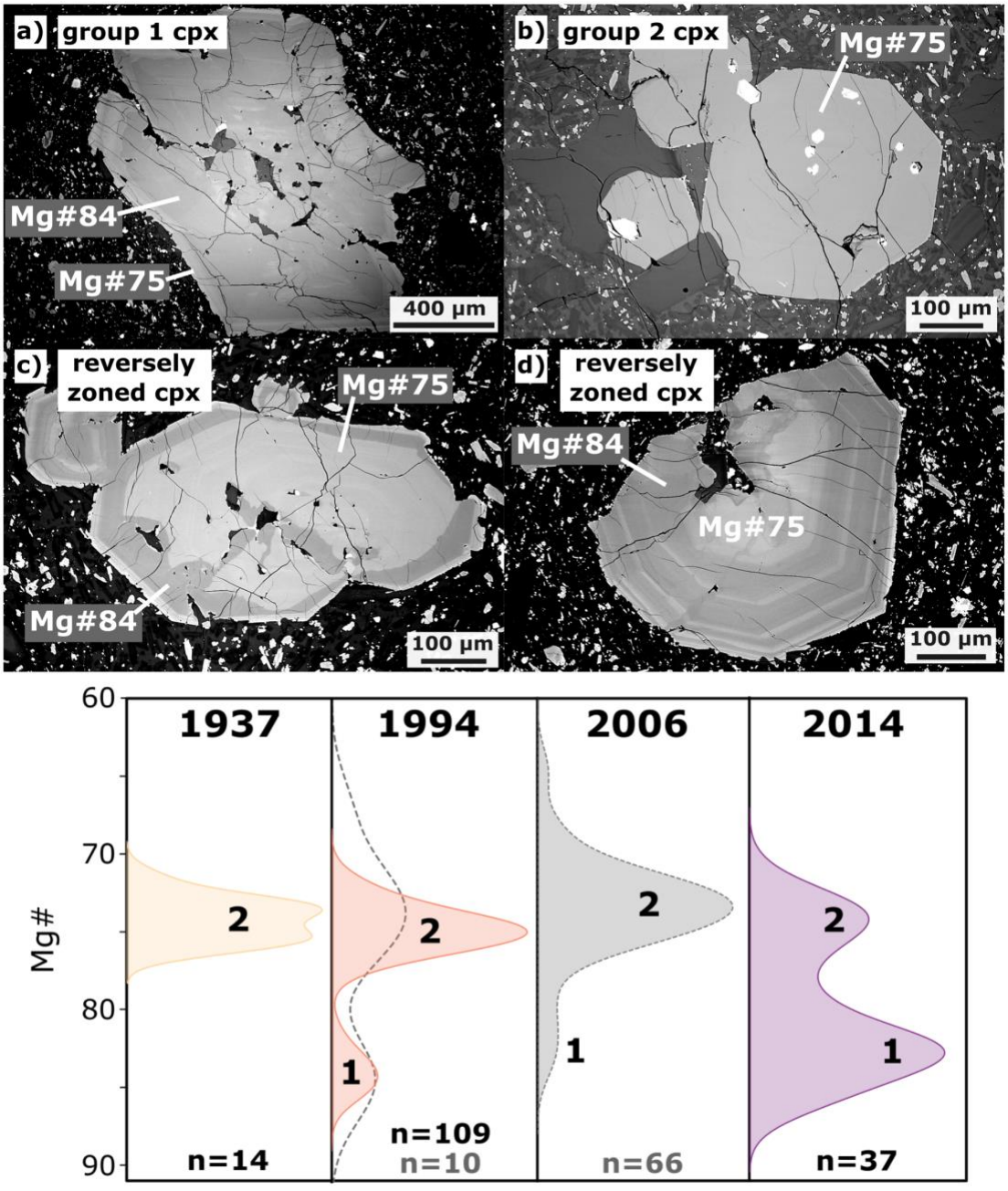

Figure 5: **Upper**: Backscattered electron images showing **a)** group one clinopyroxene with a low-Mg# rim, **b)** group two clinopyroxene, **c–d)** group two clinopyroxene with reverse zoning in the 1994 eruption products. **Lower**: Frequency plots showing the distribution of clinopyroxene core compositions from the different eruptions of Rabaul. The numbers mark the peaks of group one and group two clinopyroxene cores. Coloured shaded curves are data from this study; grey dotted curves are literature data (Bouvet de Maisonneuve *et al.*, 2015, Cunningham *et al.*, 2009, Heming, 1977, Patia, 2004). Number of analyses are given in black (this study) and grey (literature data).

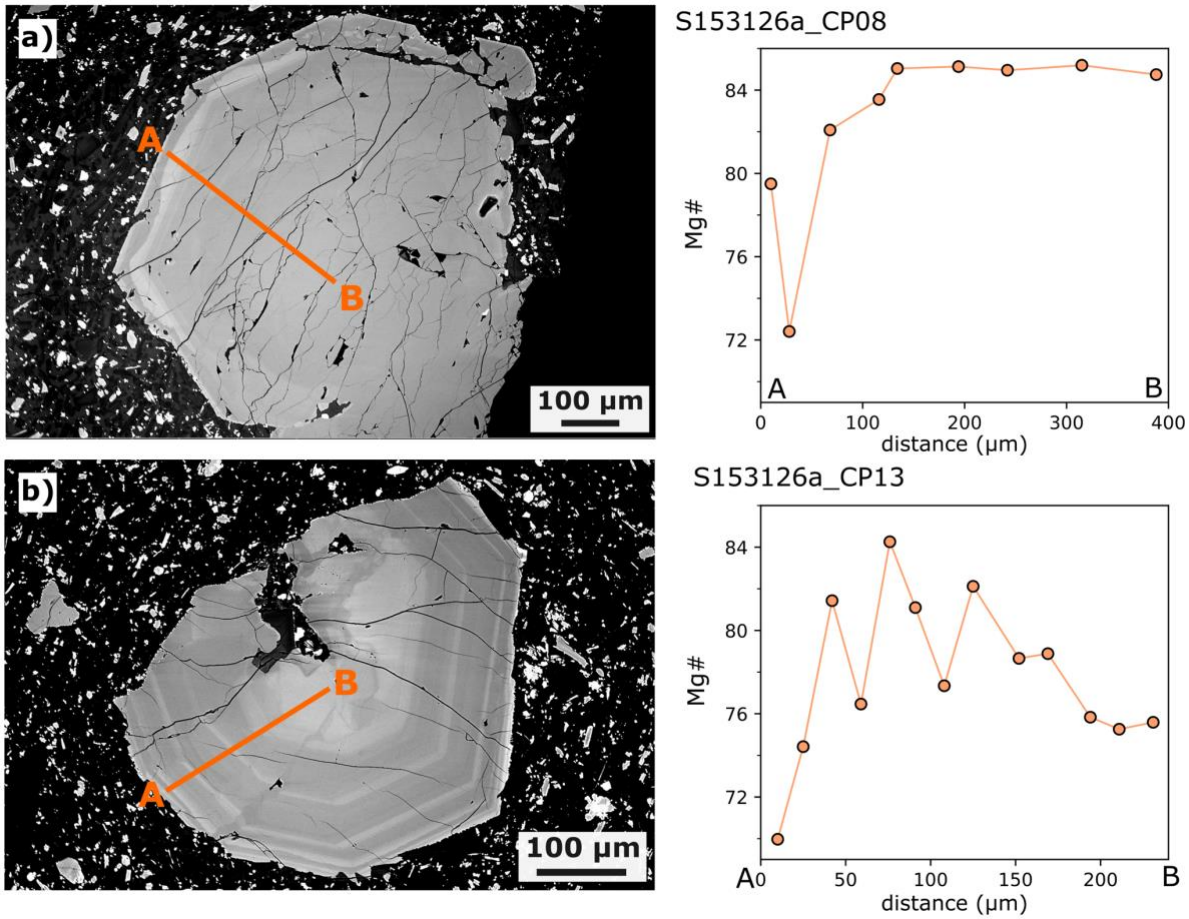

Figure 6: Examples of compositional zoning profiles across clinopyroxene from the 1994 Rabaul eruptions. **a)** Group one clinopyroxene with a rim that is lower in Mg# content, **b)** reversely zoned clinopyroxene with a group 2 core and overgrown by alternating bands of group 1 and group 2 clinopyroxene. Orange lines across crystals mark the locations of profiles.

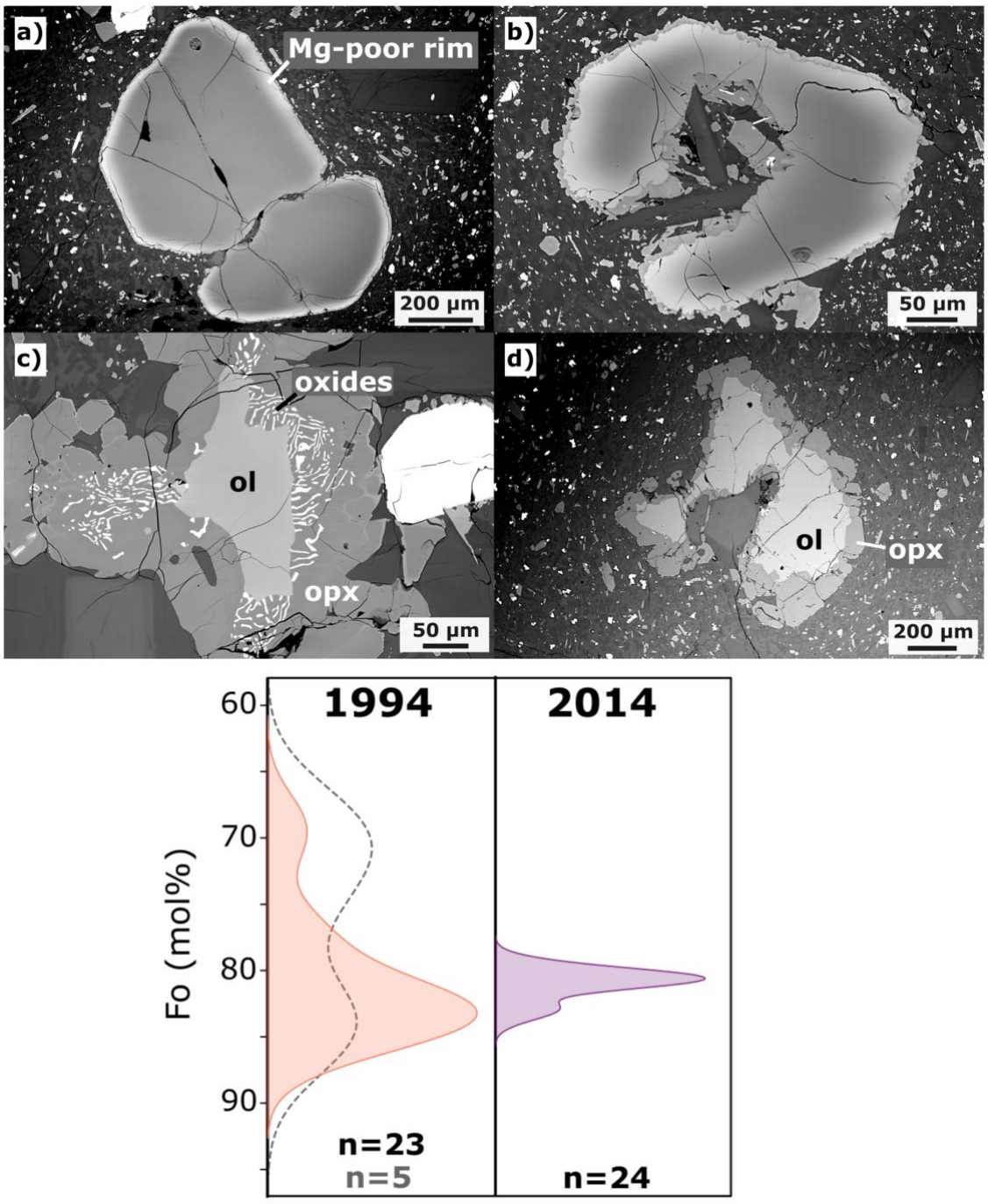

Figure 7: **Upper**: Backscattered electron images showing **a–b)** olivine with thin, Mg-poor rim; **c–d)** olivine (ol) replaced by orthopyroxene (opx). All images are of 1994 Rabaul eruption products. **Lower**: Frequency plots showing the distribution of olivine core compositions from the different eruptions of Rabaul. Coloured shaded curves are data from this study; grey dotted curves are literature data (Cunningham *et al.*, 2009, Heming, 1977, Patia, 2004). Number of analyses are given in black (this study) and grey (literature data).

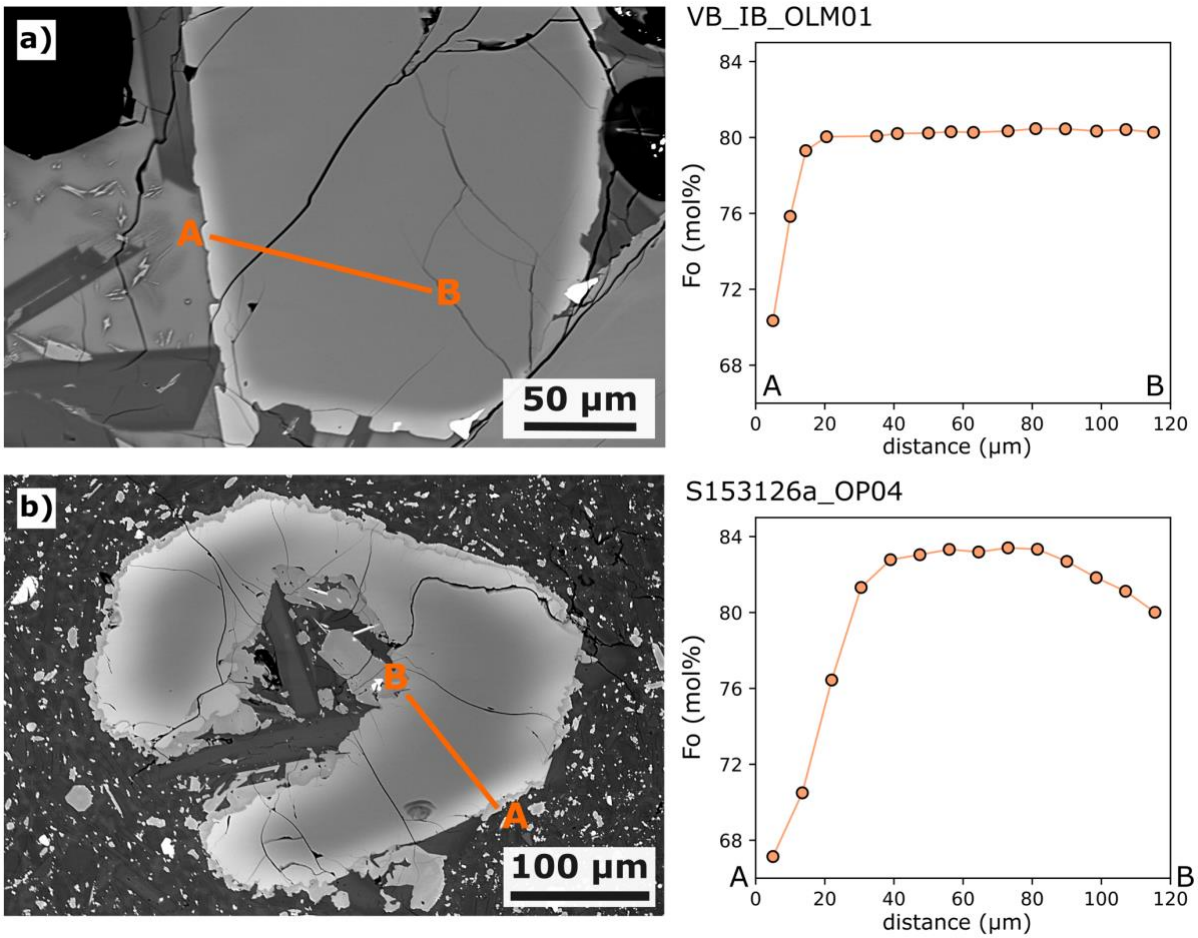

Figure 8: Examples of compositional zoning profiles across olivine crystals from the Rabaul eruptions in olivine with thin, bright, Mg-poor rim from **a)** the 2014 and **b)** eruption products. Orange lines across crystals mark the locations of profiles.

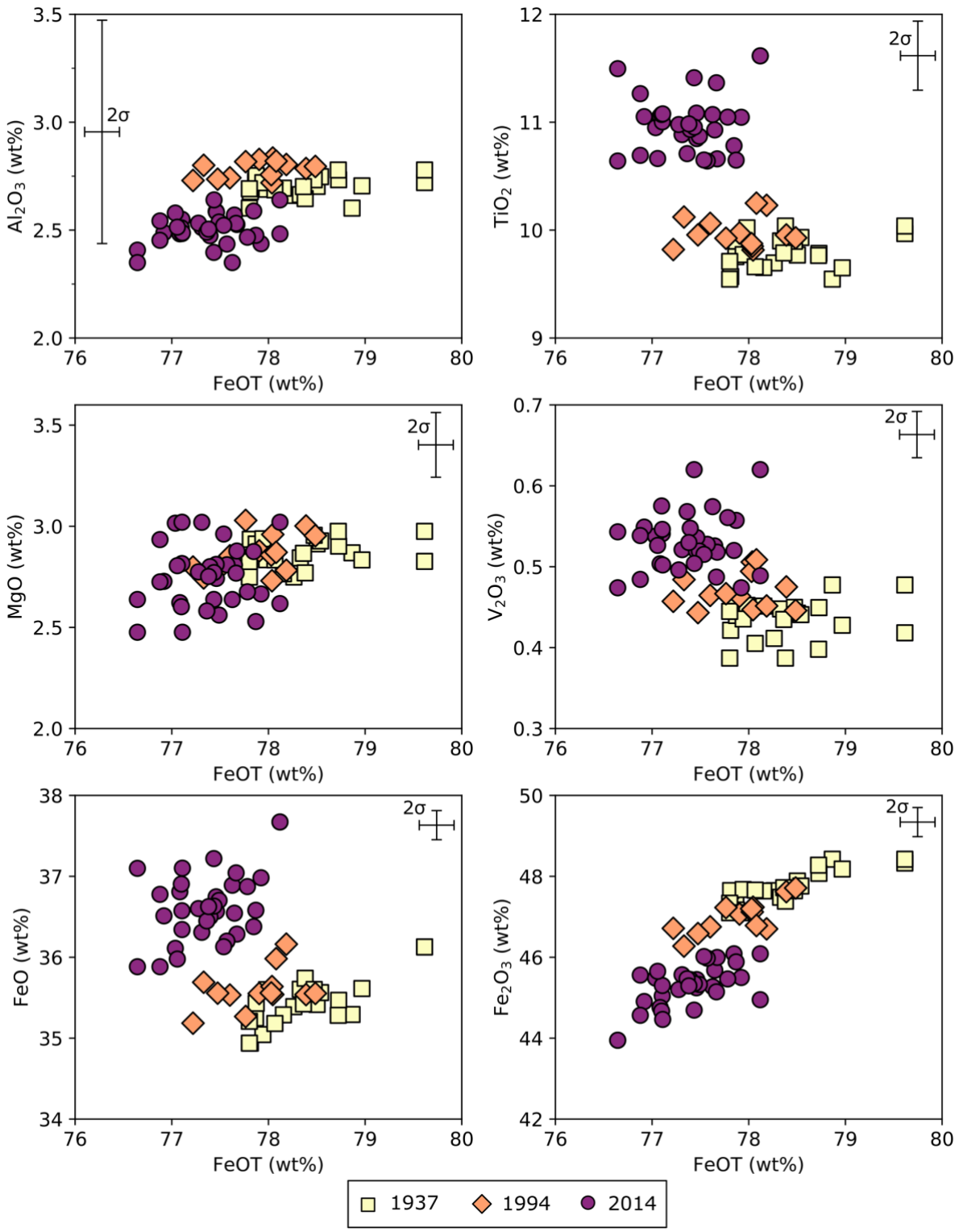

Figure 9: Ti-magnetite compositions in the 1937, 1994 and 2014 eruption products of Rabaul. Error bars indicate 2σ uncertainties.

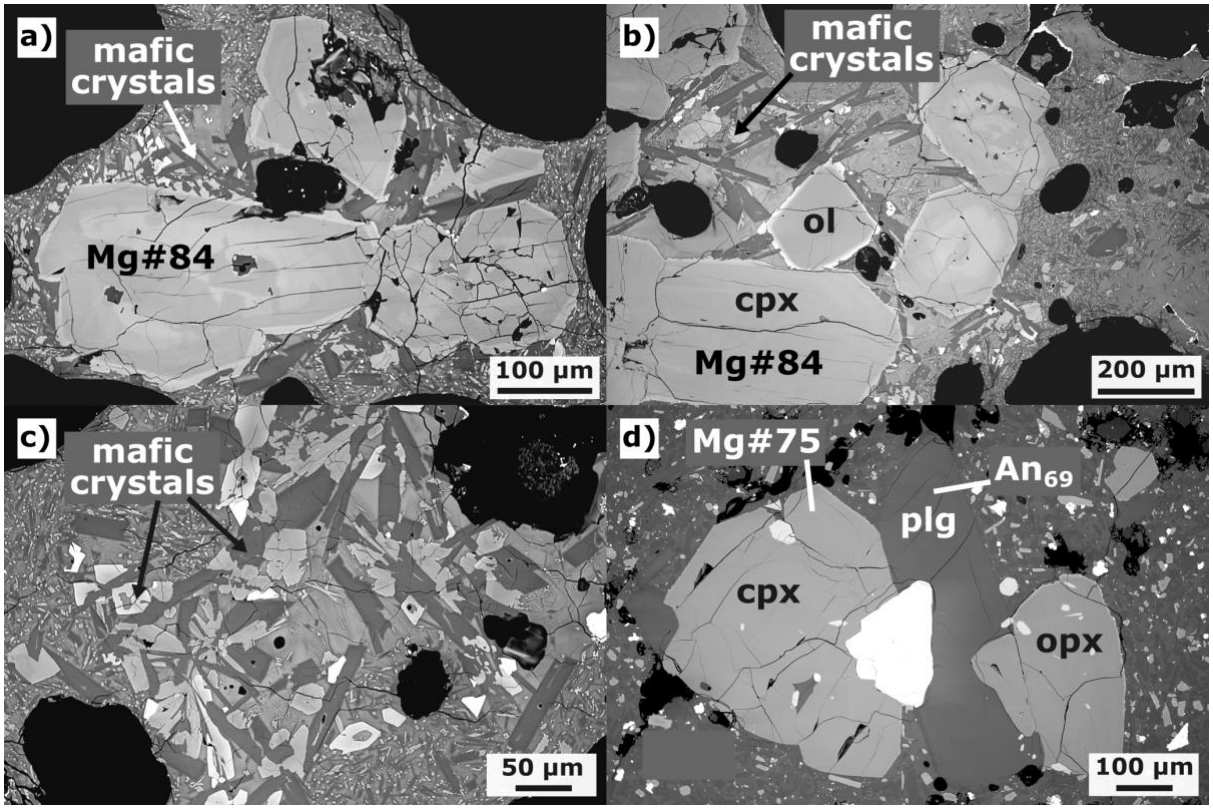

Figure 10: Backscattered electron images showing **a)** mafic mineral clot surrounded by olivine, plagioclase and clinopyroxene clusters with mafic compositions, **b)** edge of mafic mineral clot rimmed by olivine, clinopyroxene and plagioclase clusters, **c)** clusters of small olivine, plagioclase and clinopyroxene crystals with mafic compositions, all in products of the 2014 eruption. **d)** Intermediate mineral clot with group two clinopyroxene, Ti-magnetite, group three plagioclase and orthopyroxene (from left to right) in 1994 Rabaul eruption products.

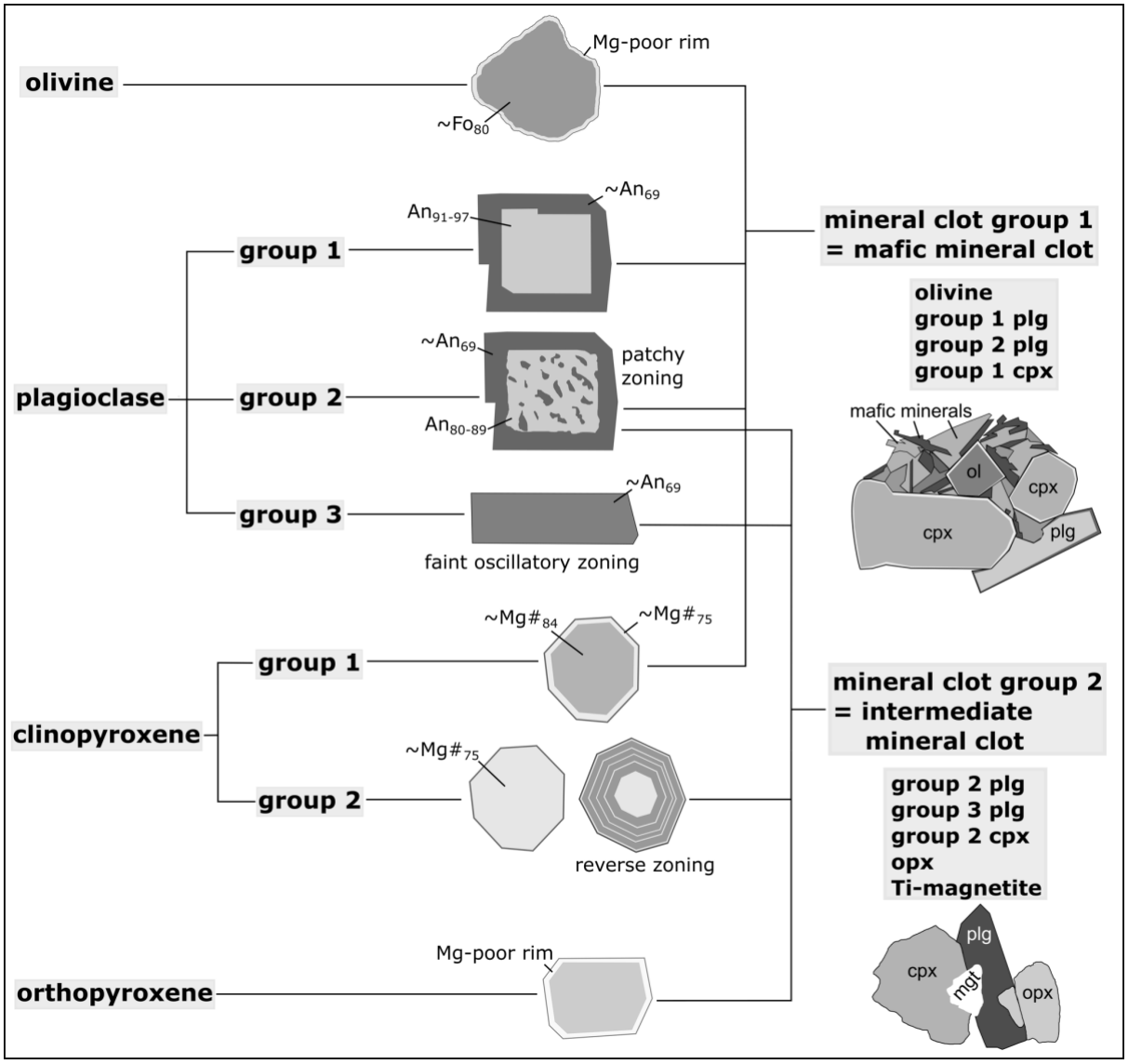

Figure 11: Sketch showing the different textural/chemical groups of macrocrysts in the Rabaul eruption products and how they can be found together in the two different groups of mineral clots. plg = plagioclase, cpx = clinopyroxene, opx = orthopyroxene.

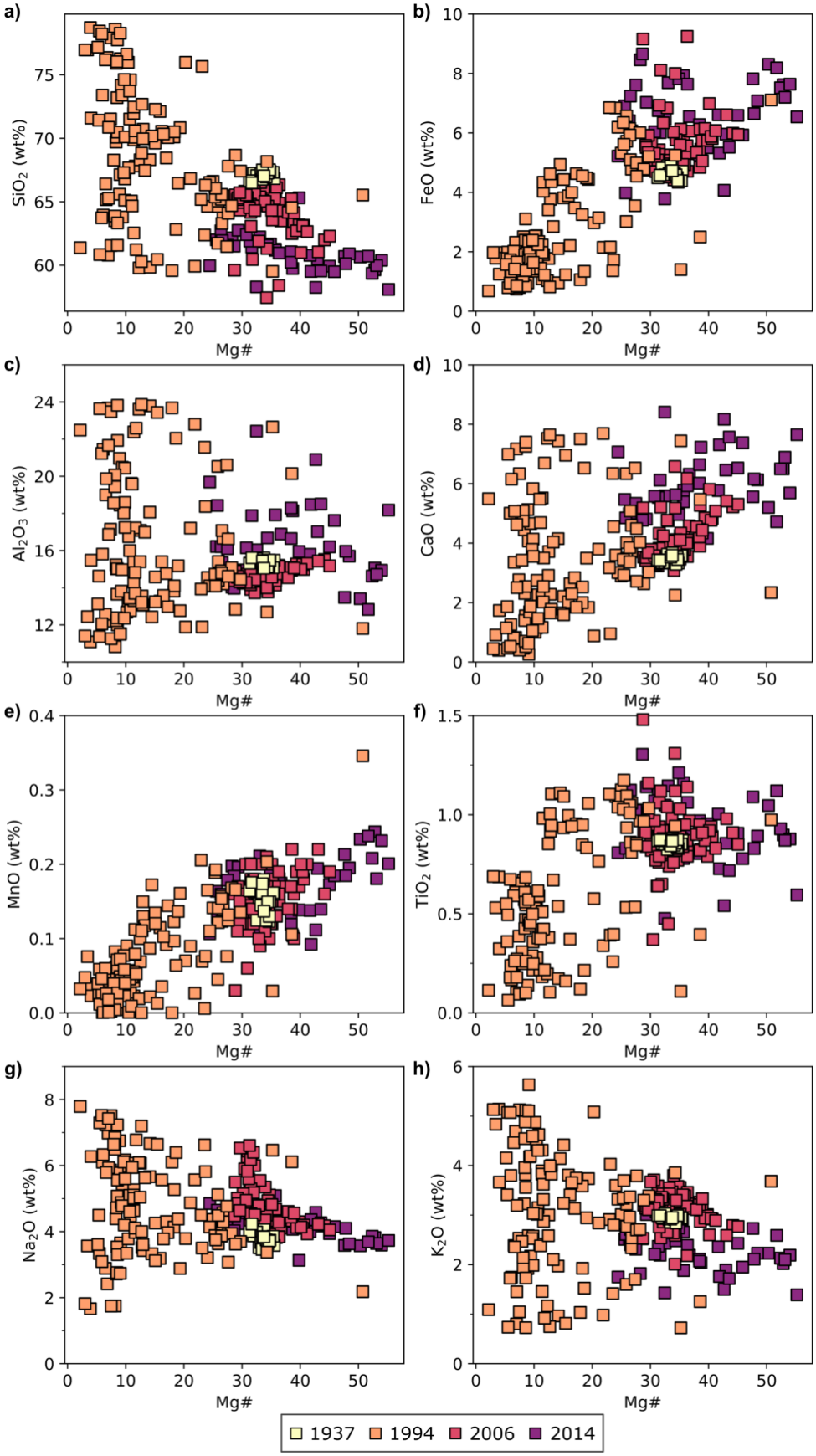

Figure 12: Matrix glass compositions from the 1937, 1994, 2006 and 2014 eruption products of Rabaul (data for 2006 eruption from Bouvet de Maisonneuve *et al.*, 2015).

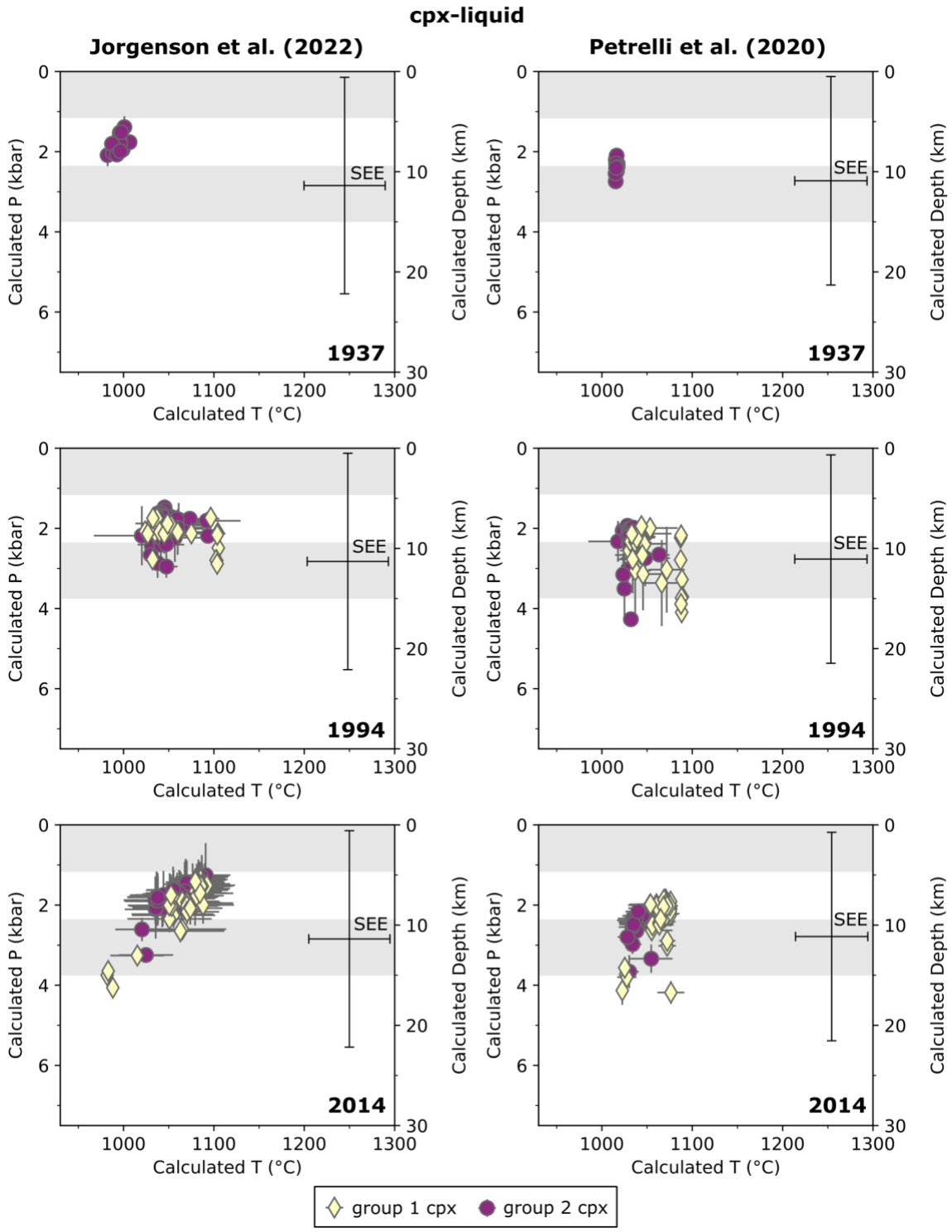

Figure 13: Cpx-liquid pressure-temperature results (group one cpx in yellow diamonds, group two cpx in purple circles) for the 1937, 1994 and 2014 eruptions of Rabaul calculated with the thermobarometry models of Jorgenson et al. (2022) (left) and Petrelli et al. (2020) (right) implemented in Thermobar (Wieser *et al.*, 2022). A H_2O content of 2.5 wt% was assumed for calculations with the models of Petrelli et al. (2020). Diamonds/circles and error bars represent mean and standard deviation of all P-T estimates for one individual clinopyroxene crystal. Standard error estimates (SEE) for the thermobarometry models are shown with the crosses. The grey bars indicate low velocity zones in a depth of 0–4 km and 9–15 km (Bai & Greenhalgh, 2005).

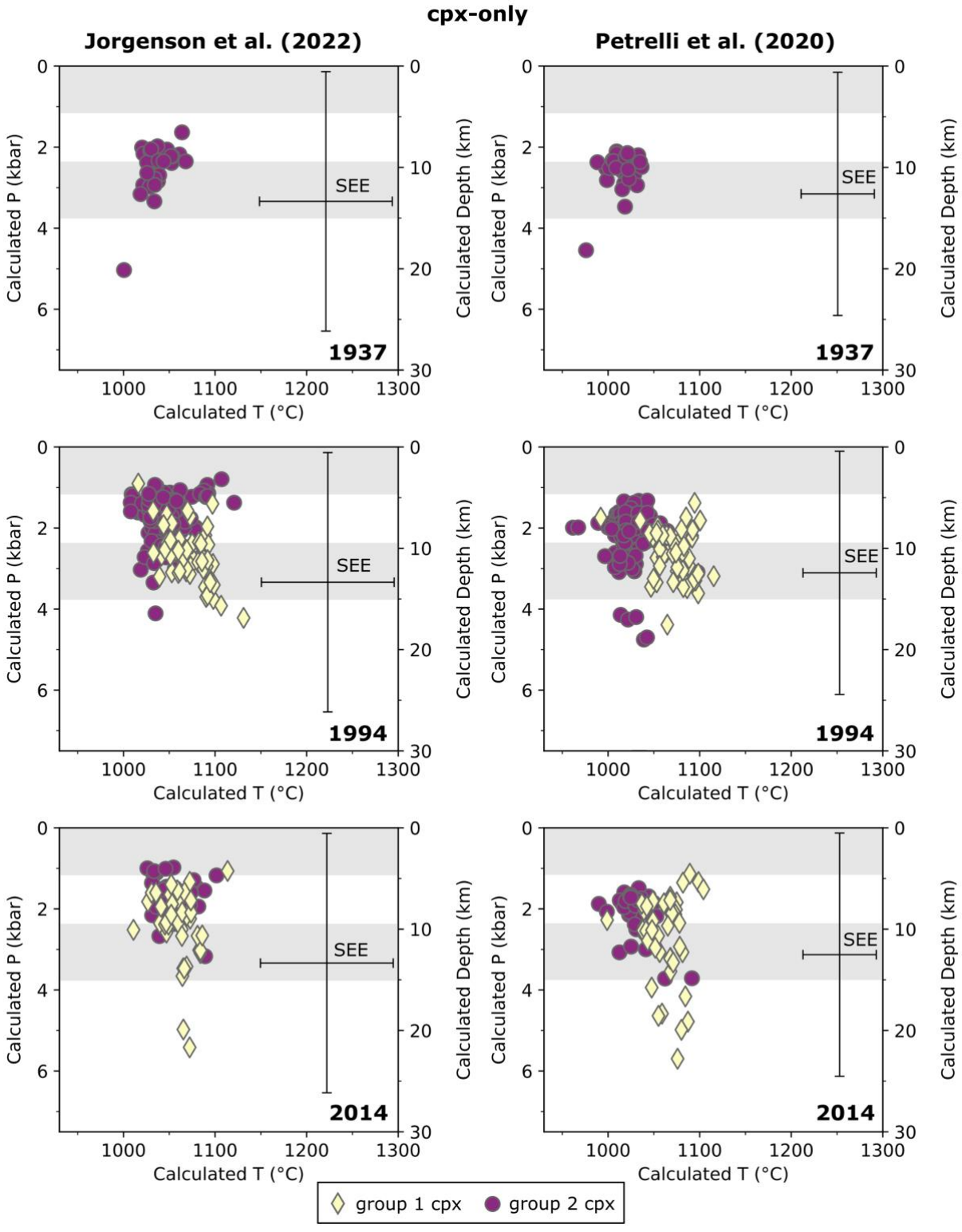

Figure 14: Cpx-only pressure-temperature results (group one cpx in yellow diamonds, group two cpx in purple circles) for the 1937, 1994 and 2014 eruptions of Rabaul calculated with the thermobarometry models of Jorgenson et al. (2022) (left) and Petrelli et al. (2020) (right) implemented in Thermobar (Wieser *et al.*, 2022). A H_2O content of 2.5 wt% was assumed for calculations with the models of Petrelli et al. (2020). Standard error estimates (SEE) for the thermobarometry models are shown with the crosses. The grey bars indicate low velocity zones in a depth of 0–4 km and 9–15 km (Bai & Greenhalgh, 2005).

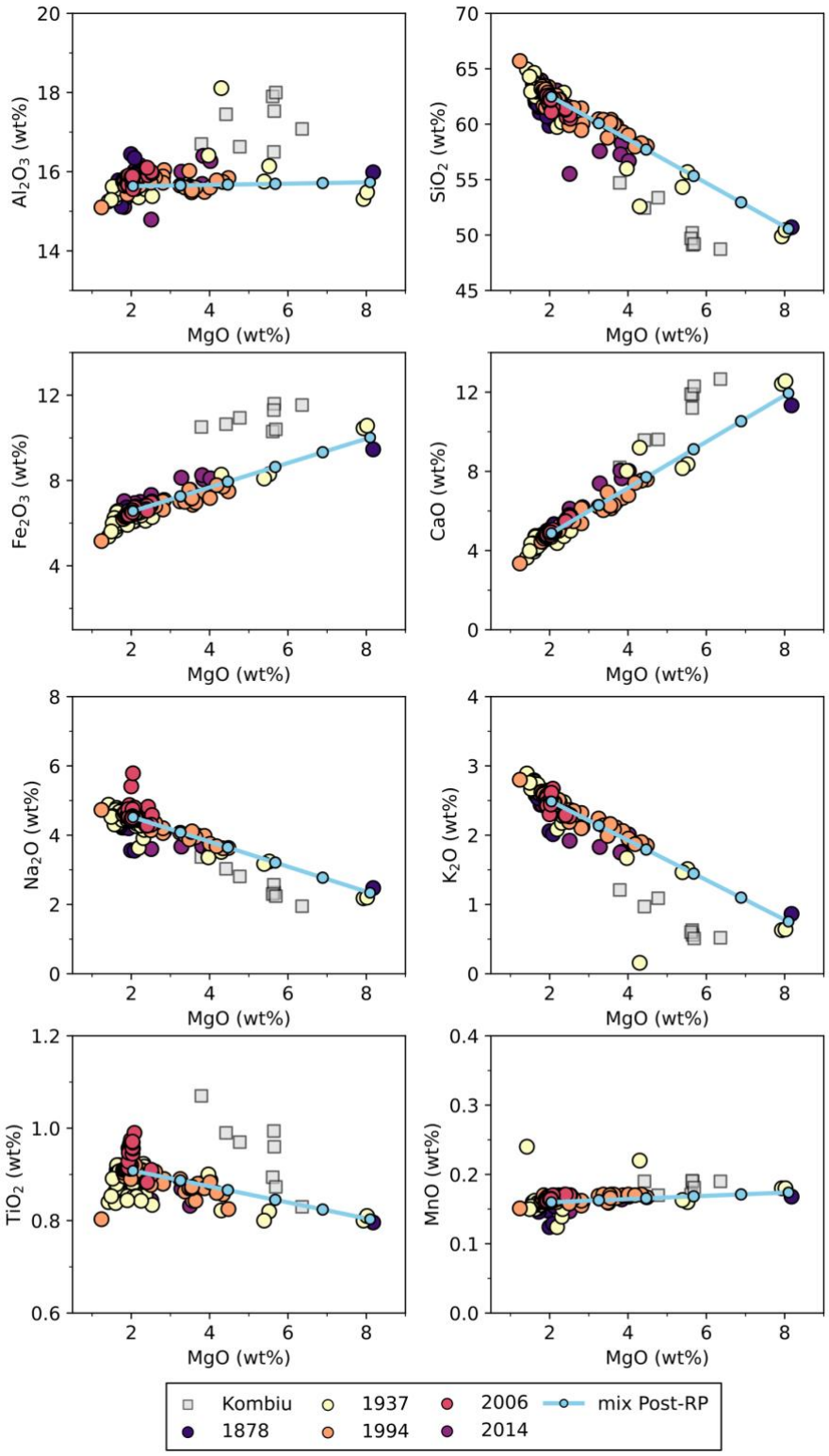

Figure 15: Diagrams showing whole rock compositions for the 1878, 1937, 1994, 2006 and 2014 eruptions of Rabaul and for the Kombiu volcano (literature data from Bernard & Bouvet de Maisonneuve, 2020, Bouvet de Maisonneuve *et al.*, 2015, Cunningham *et al.*, 2009, Fabbro *et al.*, 2020, Heming, 1974, Hohl *et al.*, 2022, Nairn *et al.*, 1989, Patia, 2004, Patia *et al.*, 2017). The light blue line is the mixing line between the average of the most primitive compositions known from the Rabaul eruptions and an average dacitic composition from the Rabaul Pyroclastics (Table 3). The light blue circles on the mixing line show mixing in 20% intervals.

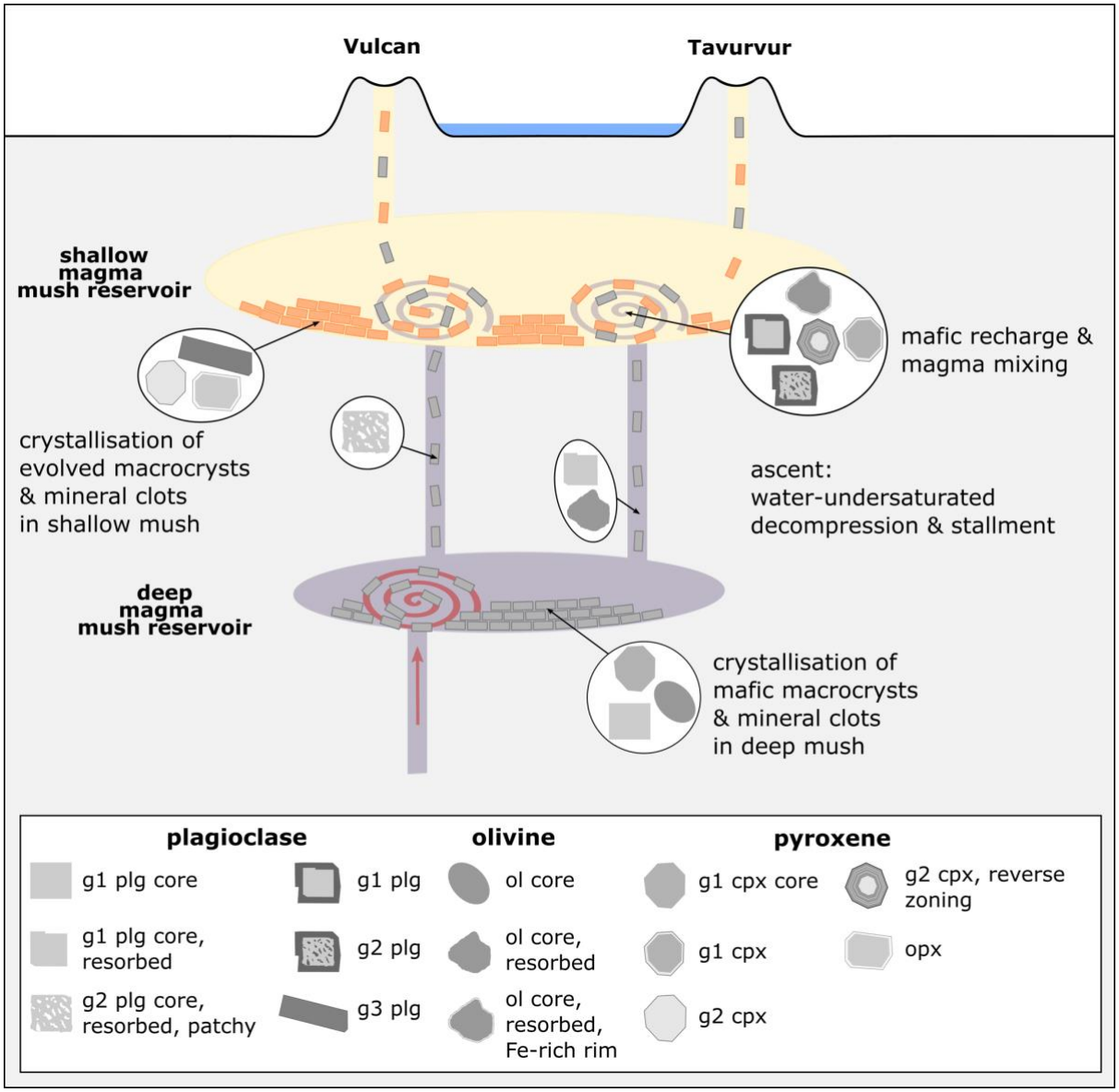

Figure 16: Revised model for the Rabaul magma plumbing system showing how the different mineral chemistries and textures found in the Rabaul eruption products formed. g = group, plg = plagioclase, cpx = clinopyroxene, opx = orthopyroxene.